Relationship of thermal boundary conductance to structure from an analytical model plus molecular dynamics simulations

Xiao Wang Zhou, Reese E. Jones, Christopher James Kimmer, John C. Duda, and Patrick E. Hopkins

Phys. Rev. B **87**, 094303 — Published 11 March 2013

DOI: 10.1103/PhysRevB.87.094303

Thermal boundary conductance vs. structure relationships derived from highly-converged molecular dynamics simulations

X. W. Zhou (Xiao Wang Zhou),[1,*] R. E. Jones (Reese E. Jones),[1] C. J. Kimmer (Christopher James Kimmer),[2] J. C. Duda (John C. Duda),[3,4] and P. E. Hopkins (Patrick E. Hopkins)[3]

[1]*Mechanics of Materials Department, Sandia National Laboratories, Livermore, California 94550, USA*
[2]*School of Natural Sciences, Indiana University Southeast, New Albany, Indiana 47150, USA*
[3]*Department of Mechanical and Aerospace Engineering, University of Virginia, Charlottesville, Virginia 22904, USA*
[4]*Microscale Science and Technology Department, Sandia National Laboratories, Albuquerque, New Mexico, 87185, USA*

(Dated: February 26, 2013)

Thermal boundary resistance dominates the overall resistance of nanosystems. This effect can be utilized to improve the figure of merit of thermoelectric materials. It is also a concern for thermal failures in microelectronic devices. The interfacial resistance sensitively depends on many interrelated structural details including material properties of the two layers, the system dimensions, the interfacial morphology, and the defect concentrations near the interface. The lack of an analytical understanding of these dependences has been a major hurdle for a science-based design of optimum systems on a nanoscale. Here we have combined an analytical model with extensive, highly-converged direct method molecular dynamics simulations to derive analytical relationships between interfacial thermal boundary resistance and structural features. We discover that thermal boundary resistance linearly decreases with total interfacial area that can be modified by interfacial roughening. This finding is further elucidated using wave packet analysis and local density of state calculations.

PACS numbers:

I. INTRODUCTION

The interface between different material layers exerts a resistance to the thermal conduction. This is manifested by an abrupt change of temperature across the two materials when a heat flux passes through[1,2]. The corresponding interfacial resistance, known as Kapitza resistance, is defined as $\sigma_i = \Delta T_i/J$, where J is the heat flux, and ΔT_i is the abrupt change of the temperature at the interface. Its inverse value, $h_i = 1/\sigma_i$, is termed Kapitza conductance. The thermal boundary resistance is an important problem for nanosystems because it can dominate the overall resistance of the structure when the dimension becomes small. This phenomenon can be utilized to improve the figure of merit of thermoelectric materials[3,4]. It can also cause local temperature accumulation leading to thermal failures in microelectronic devices.

Atomic-scale engineering of interfaces for specific thermal applications has been an elusive goal because Kapitza conductance is extremely sensitive to many structural details at the interface, including crystallinity, crystallographic orientation, roughness, interdiffusion, and chemical reaction[5,5–12]. These structural details become more important on a nanoscale because when the characteristic dimensions are comparable to or less than the phonon mean-free-paths, the interfacial scattering increases[6]. Unfortunately, interfacial thermal transport experiments are extremely challenging, and only recently have experimental studies begun to address some relationships between Kapitza conductance and microstructural features of interfaces[5,10,11,13–15]. Due to the lack of understanding of dependence of Kapitza conductance on structural details, the design of devices has typically relied on a trial-and-error approach rather than a science-based optimization.

Without requiring assumptions other than an interatomic potential that can be parameterized from fundamental bonding properties of atoms, molecular dynamics (MD) simulations are effective to explore thermal transportation and to examine effects of atomic details of interfacial structures. For instance, MD simulations have been applied to calculate thermal conductivity of superlattices[16–20]. In particular, Termentzidis et al.[17] explored the cross-plane conductivity of superlattices with a variety of interface conformations, similar to part of the current study. Although superlattices are composed of interfaces, the calculated temperature profiles do not show contributions of thermal boundary resistance of individual interfaces to the overall thermal resistivity of the material. On the other hand, MD simulations have been successfully used to directly calculate thermal boundary resistance[21–27]. These studies established the effects of sizes[28–31], temperature[21,26,32], mass differential of the two layers[21,26,27], lattice mismatch between layers[26,27], interfacial defects[26,27], stiffness of the materials, and bond strength at the interface[22,24,32,33]. While the MD data provided knowledge significantly beyond that achieved from analytical models (e.g., the acoustic mismatch model and the diffuse mismatch model[2,9]), our current understanding of the thermal boundary conduc-

tance is far from the material/structure design requirement. In particular, analytical relationships between Kapitza conductance and structural details such as interfacial morphology, interfacial defects, and coherence (the probability materials share common lattice sites) of the interface have not been established in the past MD simulations. Here we combined an analytical model with systematic MD simulations of interfacial thermal boundary transport using the "direct method" to establish analytical equations for Kapitza conductance as a function of interfacial morphology. The effects of defects, interfacial coherence, and elastic constants of the materials are also explored. Care has been taken to distinguish our work from previous studies. For instance, we will significantly expand the time scale used in the previous MD simulations (up to only several ns)[21–27] to more than 100 ns so that highly-converged MD data can be generated for verifying the analytical relationships between Kapitza conductance and structural features. In addition, we will ensure the generality of the results by using three different interatomic potentials. Finally, wave packet analysis[22,23] and local density of state calculations are performed to further elucidate the results. These studies can directly benefit current efforts to increase the figure of merit of thermoelectric nanomaterials through interface roughening[6,34–36] as well as to manage thermal transport at metalized semiconductor interfaces such as Schottky barriers and Ohmic contacts[37].

II. METHOD

A. Interatomic potential

One key objective of the present work is to gain a generic understanding of interfacial morphology effects on Kapitza conductance of metal-on-semiconductor structures. To achieve this, we will use three different potentials to ensure the generality of the results. First, we develop a Stillinger-Weber (SW)[38] type of Al-Ga-N potential interatomic potential as described in details in Appendix A. This SW Al-Ga-N will be used in a majority of our metal-on-semiconductor (Al-on-GaN) simulations. Next, we develop a hybrid embedded atom method (EAM)[39,40] + SW potential for the Al-Ga-N system, and use it in some selected (again Al-on-GaN) simulations to test the generality of the results. This potential, termed the ESW potential, is described in details in Appendix B. Finally, a Lennard-Jones (LJ) potential is used to study a mass-mismatched model A/B interface. This not only further tests the generality of the studies, but also facilitates the interpretation of the results with a simpler LJ system.

B. Direct method molecular dynamics model

In this work, we study the interfacial structure effects through simulations of phonon heat transport using a prototyping Al-on-GaN bilayer system. A two-temperature model (TTM)[41,42], which incorporates the electron heat transport, is also being applied to study the system size effects of the Al-on-GaN system. Details of the TTM studies will be summarized in a separate report[28]. Here our choice of probing the structural dependence of thermal boundary conductance via only the phonon interactions is based on the following considerations. First, some experiments indicated that electrons do not significantly affect thermal boundary conductance[7] unless in a highly nonequilibrium regime[43]. Although previous theoretical work[44,45] suggested that electrons affect the absolute values of interfacial conductance, our preliminary TTM simulations showed that electrons do not alter the trends of the conductance with respect to system geometry (e.g., the system dimensions in both cross section and transport directions). As a result, including only the phonon effect in simulations should reveal the correct structural dependence of conductivity. It also allows us to redirect our computing resources for more thorough studies at reduced statistical uncertainties.

For the Al/GaN simulations, an illustration of our computational crystal used in the direct method MD simulations is shown in Fig. 1(a), where the left side is Al and the right side is GaN. Here we assume that the [111] Al and the [0001] GaN are aligned in the $x-$ direction, the $[\bar{1}\bar{1}2]$ Al and the $[\bar{1}100]$ GaN are aligned in the $y-$ direction, and the $[2\bar{2}0]$ Al and the $[11\bar{2}0]$ GaN are aligned in the $z-$ direction. The [0001] ($x-$) direction of an GaN wurtzite (wz) crystal is stacked with alternating Ga and N planes of alternating short and large spacings, as illustrated in the inset of Fig. 1(a). Our model generally assumes that Al is in contact with Ga. For a stable interface, we further assume that the next N plane has a short spacing with the contact Ga. Two special cases are also explored. In the first case, Ga and N atoms are switched so that Al is in contact with N. In the second case, the Al is also in contact with N but the next Ga plane has a long spacing with the contact N (i.e., Ga and N atoms are not switched but the interface location is shifted). The length, width, and thickness of the system are represented respectively by L_{Al}, W_{Al}, and t_{Al} for Al and L_{GaN}, W_{GaN}, and t_{GaN} for GaN. For convenience, the dimensions are also represented by number of cells in the $x-$, $y-$, and $z-$ directions as $n_{x,Al}$, $n_{y,Al}$, $n_{z,Al}$ for Al and $n_{x,GaN}$, $n_{y,GaN}$, $n_{z,GaN}$ for GaN. Al has an fcc crystal structure with a lattice constant of $a_{Al} = 4.05$ Å (density $\rho_{Al} \approx 0.0602$ atoms/Å^3), and GaN has a wurtzite crystal structure with lattice constants of $a_{GaN} = 3.19$ Å and $c_{GaN} = 5.20$ Å (density $\rho_{GaN} \approx 0.0873$ atoms/Å^3). The

smallest orthogonal cell of Al is $a_{x,Al} = \sqrt{3} \cdot a_{Al}$, $a_{y,Al} = 0.5\sqrt{6} \cdot a_{Al}$, and $a_{z,Al} = 0.5\sqrt{2} \cdot a_{Al}$. The smallest orthogonal cell of GaN is $a_{x,GaN} = c_{GaN}$, $a_{y,GaN} = 2cos(\pi/6) \cdot a_{GaN}$, $a_{z,GaN} = a_{GaN}$. These mean that $L_{Al} = n_{x,Al} \cdot a_{x,Al}$, $t_{Al} = n_{y,Al} \cdot a_{y,Al}$, $W_{Al} = n_{z,Al} \cdot a_{z,Al}$, $L_{GaN} = n_{x,GaN} \cdot a_{x,GaN}$, $t_{GaN} = n_{y,GaN} \cdot a_{y,GaN}$, $W_{GaN} = n_{z,GaN} \cdot a_{z,GaN}$. Obviously, while the (111) Al and (0001) GaN cross-section planes are both hexagonal, the cross-section dimension of the system must be constrained so that $W_{Al} \approx W_{GaN} \approx W$, and $t_{Al} \approx t_{GaN} \approx t$. Here we use standard cross-section of $n_{y,Al} = 29$, $n_{z,Al} = 10$, $n_{y,GaN} = 26$, and $n_{z,GaN} = 9$. These combinations of numbers of Al and GaN cells in the cross-section dimensions produce low Al/GaN lattice mismatch strains of ϵ_y = 0.001 in the $y-$ direction and ϵ_z = -0.003 in the $z-$ direction. In particular, ϵ_z = -0.003 is also the minimum misfit strain for any combinations of number of Al and GaN cells in the $z-$ direction when $n_{z,Al} \leq 28$, so that the misfit strain ϵ_z will not be further reduced even when the $z-$ dimension is more than doubled. To give a further quantification of the misfit effect, the relative $(y-z)$ biaxial stress calculated from a typical sample is plotted along the $x-$ direction in Fig. 1(b). Here the relative stress means that the absolute stresses of Al and GaN are scaled respectively by the average magnitudes of the stresses in the Al and GaN bulk, respectively. It can be seen from Fig. 1(b) that the contribution to stress from the interface is no more than twice of that from the surfaces.

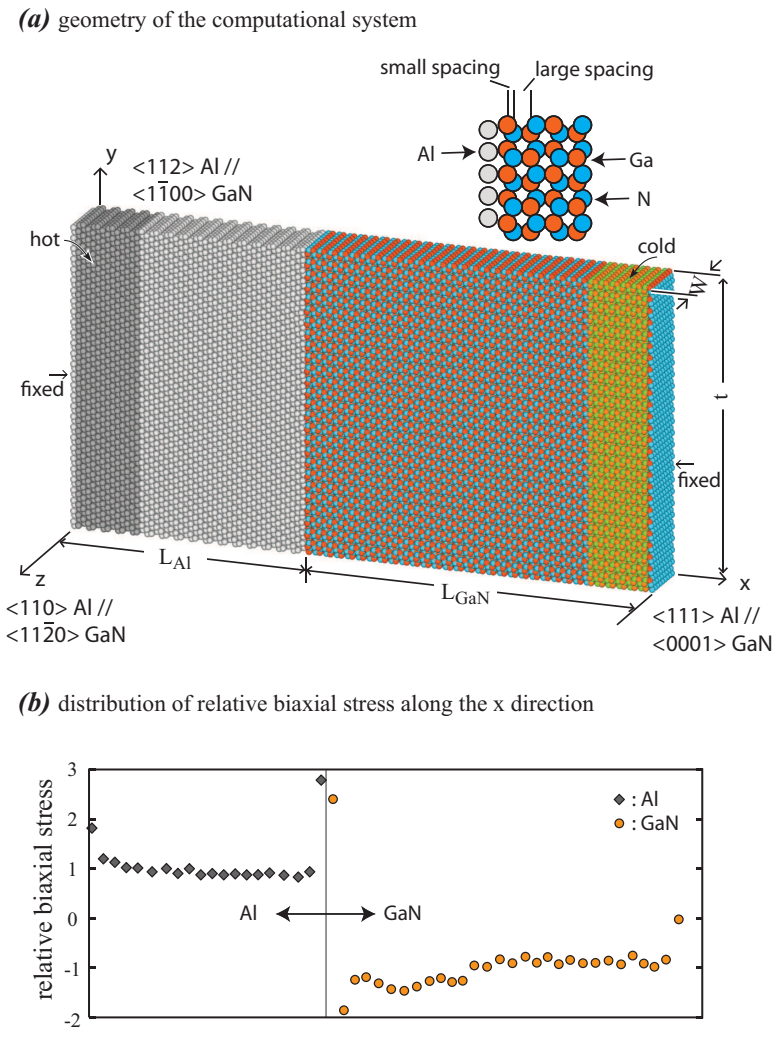

FIG. 1: (Color online) (a) Computational crystal used in the direct method MD simulations, and (b) distribution of the relative $(y-z)$ biaxial stress in the $x-$ direction. Here the relative stresses of Al and GaN are scaled respectively by the average magnitudes of the stresses in the Al and GaN bulk, respectively.

The computational crystal with the desired dimension is first created based on the 0 K temperature lattice constants of the materials. Tentative strains in the cross-section directions are applied to the two material layers to compensate for the lattice mismatch. To relax the tentative strains and to incorporate the thermal expansion effect, a pre-conditioning MD simulation is performed at the simulated temperature (via velocity rescaling) for a designated time (e.g., 20 ps or more) using a zero-pressure NPT (constant number of atoms, pressure, and temperature) periodic

boundary conditions in all three coordinate directions. After discarding the simulation for the first half of time, the average dimensions obtained during the last half of time are then used to create a new crystal with the thermal expansion effect incorporated (for the SW potential at 300 K, the thermally relaxed crystals typically have normal strains of 0.0013, 0.0013, 0.0013 for GaN and 0.0012, 0.0001, and 0.0034 for Al in the three coordinate directions as compared to their equilibrium sizes at zero K). This crystal is used in the main MD simulation of thermal transport.

In the main MD simulations, periodic boundary conditions are used in the $y-$ and $z-$ directions such that simulated systems approximate an infinite cross-section area. A non-periodic boundary condition is used in the $x-$ direction to enable non-symmetric interfacial geometry. To ensure that the system is kept at the thermally-expanded dimension, one atomic Al layer (light gray) at the left end and a pair of atomic Ga (red) and N (blue) layers at the right end, as indicated in Fig. 1, are held fixed during simulations.

During thermal transport simulations, MD is first run for a designated time (e.g., 10 ps) under the NVT (constant number of atoms, volume, and temperature) condition using velocity rescaling to set up the desired system temperature T. MD is then continued with an NVE (constant number of atoms, volume, and energy) condition while at the same time a constant heat flux is introduced[23,46–50]. Here regions with a designated width of about 30 Å immediately beside the two fixed ends, as shown in dark grey near the left side and yellow/orange near the right side in Fig. 1, are simulated as hot (heat source) and cold (heat sink) regions. This is achieved by continuously adding a constant amount of energy to the hot region and removing exactly the same amount of energy from the cold region at each MD time step using velocity rescaling (while preserving linear momentum). The simulation then naturally creates a heat flux and a temperature differential in the $x-$ direction. Here a relatively large size (30 Å) of heat source and sink is used because we found that small sizes lead to an abnormal temperature spike in the hot region and an abnormal temperature dip in the cold region. To compute the temperature profile, bins (finite element mesh) with appropriate width are generated either along the $x-$ direction (for majority of our thermal transport calculations) or along both the $x-$ and $y-$ directions (for selected study of local temperature distribution). A temperature averaged over a designated number of time steps is calculated for each of the bins. To generate extremely accurate results, the duration of the NVE simulations is chosen to be extremely long in the MD standard (e.g., at least 110.4 ns for the Al/GaN case). For reference, the majority of our simulations include ∼55,000 to ∼85,000 atoms. Note that increasing the averaging time is very effective in improving the accuracy of thermal conductivity calculations[51] where a small temperature gradient appears in the denominator of the expression. Here the denominator in the conductance expression is the temperature drop across the interface, which is larger than the temperature gradient in the conductivity calculations. As a result, accurate thermal boundary conductance results can be obtained at shorter averaging times. As will be described below, however, we found that under the simulation conditions suitable for accurate thermal boundary conductance calculations, the temperature gradients within individual material layers necessarily approach zero. This leads to uncertain thermal conductivities for individual materials, and may occasionally affect the thermal boundary conductance calculations. By using very long averaging times, on the other hand, all of our results have extremely small statistical / systematical errors. We also perform more than 20 simulations each with 1/20 averaging times. The statistical average of the conductance obtained from the 20 simulations converges almost perfectly to the result from the single, long time simulation.

After discarding the initial stage of simulation to allow the system to reach a dynamic equilibrium, the temperature profile averaged over the remaining time (at least 110 ns for the Al/GaN case) is used for analysis. Our work will focus on a relatively low temperature (300 K for the Al/GaN case and 10 K for the LJ system), although for comparison reasons selected cases are also explored at higher and lower temperatures. Note that the GaN Debye temperature estimated by different groups ranges from 350 K to 600 K[52–54]. Although 300 K is at the lower bound of the estimated Debye temperature range, we emphasize again that our objective is not to extract quantitative data for specific materials but rather to discover functional dependence of Kapitza conductance on interfacial structures. The low temperature MD simulations are beneficial for such studies as they effective reduce systematic / statistic errors[51,55,56], which is the limiting factor for discovering accurate functional dependences.

As mentioned above, simulations were performed using the fixed-boundary condition in the $x-$ direction (i.e., with the rigid ends, Fig. 1). We also explored the free-boundary condition in the $x-$ direction and it is worth discussing the results. As an example, here we assume heat conduction through an interface-free GaN (without the Al) segment with the same orientation as shown in Fig. 1. The sample dimension has $n_{x,GaN} = 152$ (≈ 790 Å), $n_{y,GaN} = 10$ (≈ 55 Å), and $n_{z,GaN} = 6$ (≈ 20 Å), and the heat flux is J = 0.0002 $eV/ps \cdot Å^2$. The temperature profiles obtained using the fixed- and the free-boundary conditions are shown respectively as the filled circles and unfilled diamonds in Fig. 2. It can be seen that the fixed-boundary condition produced an expected temperature profile (a Fourier temperature gradient) in the middle of sample whereas temperatures near the two sample ends begin to drop as these ends are essentially frozen. In contrast, the free-boundary condition produced an abnormally large temperature increase at the hot end. This was found to always occur with the constant flux method where the hot and cold regions are not thermostated. Note that the temperature calculated in MD simulations is accurate only when atom velocities satisfy a zero momentum condition. Obviously, a free surface may cause non-zero momentum in local regions near

the surface, likely to be responsible for the observed abnormal temperature distribution. Although Fig. 2 does not show a significant difference of the temperature gradients at the middle point of the sample (and hence the thermal conductivities) between the fixed- and free-boundary conditions, the abnormal temperature profile can be a source of error. This justifies our choice of fixed boundary condition.

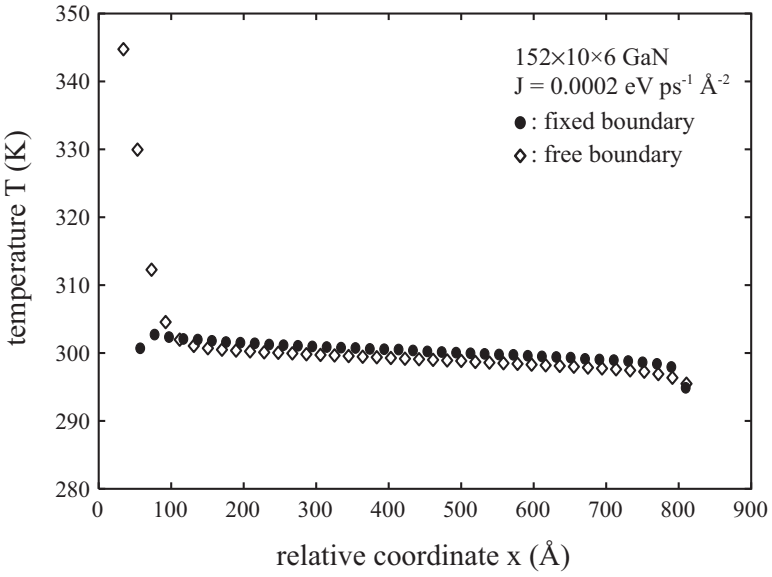

FIG. 2: Effects of fix- and free-boundary conditions on direct method MD simulations of thermal transport.

It appears that a constant temperature control method (i.e., the hot and cold regions are directly thermostated) may eliminate the abnormal temperature spike seen under the free-boundary condition. However, we found that simulations with the constant temperature method are either unstable when the temperature in the thermostated regions are equilibrated too quickly (e.g., scaled the atom velocity every time step), or the results depend on the input parameter characteristic of the equilibration time (e.g., the damping parameter in the Nose-Hoover method[57]). Considering that the literature predominantly uses the constant flux method, we do not further explore the constant temperature method.

III. ANALYTICAL MODEL OF INTERFACIAL MORPHOLOGY

One approach that offers an enormous freedom to tailor Kapitza conductance for a given material system is to change the interfacial morphology. One of the current authors is involved in recent experiments towards this direction by introducing interfacial roughness through etching to alter the Kapitza conductance[5]. The results indicated that Kapitza conductance decreases with the roughness-promoting patterned etching as a potentially useful fabrication technique for reducing contact resistance. However, it is difficult to conclude from experiments alone if this decrease in conductance is caused by the increased roughness or by a change of the oxide layer. To elucidate the experimental observations, we focus to study the interfacial morphology effect.

To help connect to the physics when MD results are presented, we first develop an analytical model. To motivate the model, an MD simulation of thermal transport through a rough Al/GaN interface was performed. The simulated sample, shown in Fig. 3, has a length of $n_{x,Al} = 16$ and $n_{x,GaN} = 30$ (L $\approx$ 268 Å). The "rough" interface, is essentially a rectangular tooth with a depth of $\delta = 34$ Å and a width of $\lambda = 69$ Å. The kinetic energies of atoms were averaged over the 0.11 billion time steps (i.e., 110 ns duration at a time step size of 1 fs) of simulations and a bin size of 5 Å. The results were converted to temperatures and are shown in Fig. 3, where the color scheme shows the temperature and the ball size distinguishes Al from GaN. Note that our temperature is averaged over a small number of atoms within a bin size of 5 Å. As a result, the statistic temperature variation is usually very large with short MD simulations (see, e.g., Fig. 14 below). . To assist a numerical understanding of the quality of our data, an integrated (over the cross section area) temperature profile is also shown in Fig. 3. It can be seen that although the temperature color map appears to have some small perturbation inside the GaN layer (the vertical band), this oscillation is in fact extremely small as can be identified from the integrated temperature profile. The high-quality data reflects the effect of our extremely long averaging time. Fig. 3 indicates an important phenomenon: while Al and GaN have very different

temperatures, the temperature is extremely uniform inside either the Al or the GaN regardless of the presence of the tooth. This also means that the temperature exhibits a constant change at the interface. The constant temperature change between Al and GaN is strong evidence that the heat transfer from Al to GaN occurs at both the vertical and the horizontal Al/GaN interfaces. The uniform temperature distribution inside each material also indicates that the heat is fully dissipated once it transfers across either the vertical or the horizontal interfaces. This means that the bottle-neck of the heat transfer is at the interface, but not in the interior of each layer. These insights can lead to a simple analytical function of Kapitza conductance as a function of roughness depth δ as derived below.

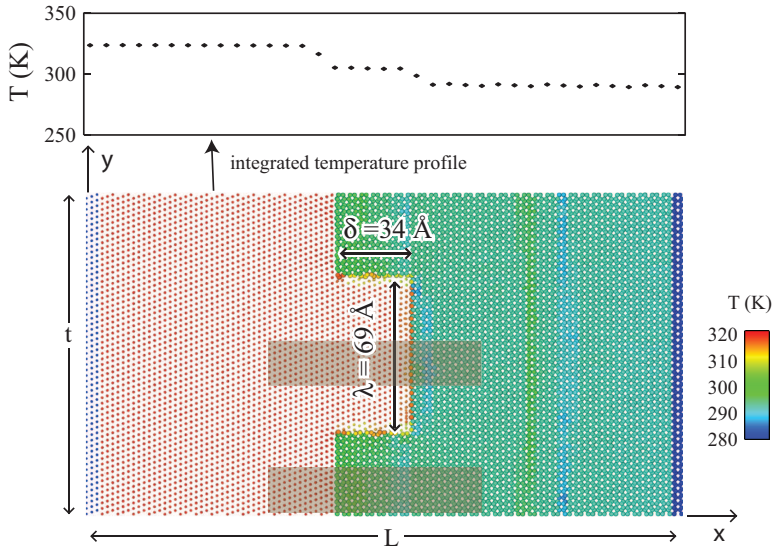

FIG. 3: (Color online) Temperature map of a "rectangle"-shaped Al/GaN interface.

Assume that the local Kapitza conductance through the vertical and the horizontal interfaces can be represented respectively as h_x and h_y. The rate of heat transfer, Q, through both vertical and the horizontal interfaces, can be expressed as

$$Q = h_x \cdot \Delta T \cdot A_x + h_y \cdot \Delta T \cdot A_y = h_x \cdot \Delta T \cdot t \cdot W + h_y \cdot \Delta T \cdot 2\delta \cdot W \tag{1}$$

where $A_x = t \cdot W$ and $A_y = 2\delta \cdot W$ are the total area of vertical and horizontal interfaces. The apparent Kapitza conductance, h, which is measured in the $x-$ direction, can then be written as

$$h = \frac{Q}{t \cdot W} \cdot \frac{1}{\Delta T} = h_x + \frac{2\delta}{t} \cdot h_y \tag{2}$$

Eq. (2) indicates that the Kapitza conductance linearly increases with δ. This finding can also be re-stated as: for defect-free, highly coherent interfaces, Kapitza conductance increases when the total interfacial area is increased. In the following more extensive MD data will be used to test the validity of this relation.

IV. RESULTS AND ANALYSIS OF AL/GAN INTERFACES

A. Effects of interfacial morphology

1. *Rectangular morphology of interfaces*

Fig. 3 already demonstrates one important phenomenon of a rectangular interface. Here we further study this interface morphology. The computational sample is assumed to have a length of $n_{x,Al} = 10$, and $n_{x,GaN} = 20$ (L $\approx$ 174 Å) along the $x-$ direction as shown in Fig. 4(a). We point out that some published MD simulations attempted

to use longer length so that the results are relatively insensitive to the dimension[21]. However our previous MD simulations have established that the Kapitza resistance is a linear function of inverse of sample length[28]. With an analytical size scaling known, here we choose to use a short length. This choice does not affect the trends of the results, but allows us to direct our computer resources to maximize averaging times, which helps reduce errors for reliably revealing functional dependence of Kapitza conductance on interfacial structures. Equally importantly, the length scale is relevant to practical applications where each layer of the multilayered devices can be as thin as a few nanometers[58].

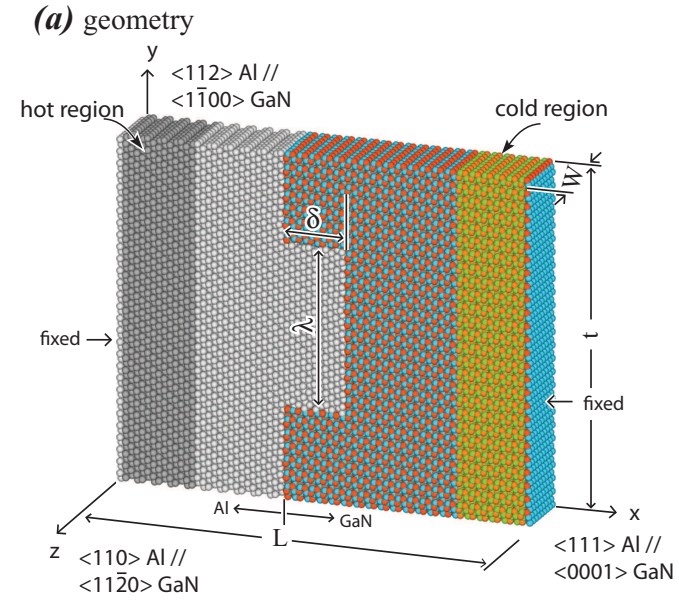

In the figure, L = 10 Al + 20 GaN cells (70 Al + 104 GaN Å),
t = 29 Al or 26 GaN cells (144 Å), W = 10 Al or 9 GaN cells (29 Å),
δ = 26 Å, λ = 69 Å

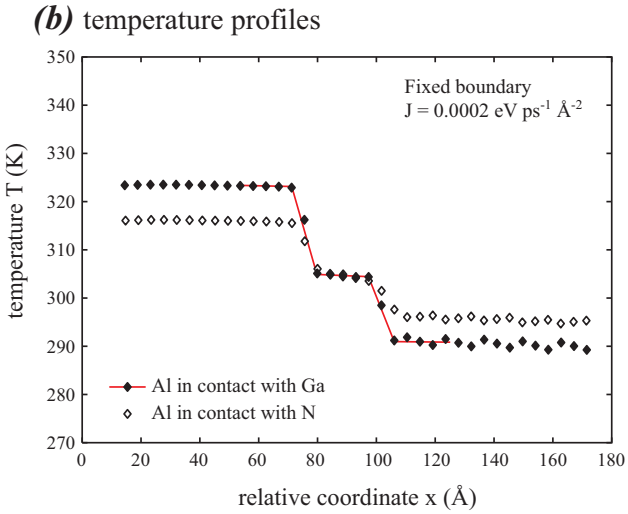

FIG. 4: (Color online) (a) Computational geometry, and (b) simulated temperature profiles across a "rectangle"-shaped interface with both the Al-Ga and Al-N contact configurations.

The rectangular interfacial morphology can be characterized by the depth δ and the lateral width λ of the tooth. In general, a larger δ corresponds to a larger interfacial area. Here we used $\delta = 26$ Å and $\lambda = 69$ Å. A direct method MD simulation was performed at a heat flux of J = 0.0002 $eV/ps \cdot Å^2$ in the $x-$ direction. The temperature profile obtained from the simulation is shown as the filled diamonds and red line in Fig. 4(b). Fig. 4(b) indicates five distinctive temperature regimes: two sharp temperature drops and three slow-decaying temperature plateaus. Clearly, the two temperature drops correspond well to the left and the right vertical Al/GaN interfaces. The slow-decaying

temperature regimes at the left and the right correspond well to the thermal transport inside the Al at the left and the GaN at the right. The slow-decaying temperature region in the middle covers a range of about 25 Å, matching well the depth of the Al tooth. Clearly, this slow-decaying region can be related to the cross-section areal average of the temperatures and thermal conductivities of Al and GaN over the tooth depth range.

One observation in Fig. 4(b) is that the temperature decay within the Al and GaN layers is extremely small. This is because the flux used in the simulations is adjusted to induce an appropriate temperature drop of around 30 K for accurate determination of interfacial conductance. As the interfacial resistance dominates the resistivity of the individual layers, this temperature drop (or flux) would necessarily produce negligible temperature decay within individual layers. This also means that the temperature profiles demonstrated in Fig. 4(b) are not appropriate to accurately calculate the thermal conductivities of Al and GaN because the near-zero temperature gradient would occur in the denominator in the conductivity expression.

As stated above, the Al/GaN structures explored here generally assume that the Al layer is in contact with the Ga atomic plane of the GaN layer. As a special case, a similar study was also conducted using the same system except that Ga and N atoms are switched so that the Al atoms are in contact with N atoms. The temperature profile thus obtained is included in Fig. 4(b) using the unfilled diamonds. Again, five distinctive temperature regimes can be identified. The overall temperature drop, however, is reduced, indicating an increase in Kapitza conductance. Based on the total temperature drop from the left Al side to the right GaN side shown in Fig. 4, we find a Kapitza conductance of h = 0.102 $GW/m^2 \cdot K$ for the Al-Ga contact case and h = 0.172 $GW/m^2 \cdot K$ for the Al-N contact case. A larger conductance for the Al-N contact can be attributed to a stronger bonding and shorter bond length between Al and N than between Ga and N[28]. Depending on the vapor phase chemical potential used in experiments, the GaN films can be Ga-terminated or N-terminated prior to the growth of Al[59]. The simulated results indicate that it might be possible to control surface termination to tune the Kapitza conductance.

To further quantify Kapitza conductance as a function of interfacial depth, simulations were performed at different values of δ between 0 and 34 Å. The computational systems used for this study have the same cross-section and the same tooth length $\lambda = 69$ Å, but the thermal transport length is increased to $n_{x,Al} = 16$ and $n_{x,GaN} = 30$ (L $\approx$ 268 Å) to accommodate the wide variation of tooth depth. A representative case is shown in Fig. 5(a) (note that the two regions shaded in blue at the lower and upper horizontal Al/GaN interfaces will be removed in separate studies of void effects, which will be described in section IV B). Selected temperature profiles at $\delta = 0$, 10, and 30 Å are shown in Fig. 5(b). Fig. 5(b) indicates that when δ is large, the left and right interfaces are widely separated so that each of them causes a separate temperature drop. Over the tooth depth range, the temperature slowly decays, representing an average thermal conductive behavior of the mixed Al and GaN region. When δ is small, the left and the right interfaces essentially overlap so that temperature exhibits only one drop at the interface as is expected for a flat interface. Fig. 5(b) also indicates that the total temperature drop from Al bulk to GaN bulk decreases when δ is increased. This indicates that the Kapitza conductance increases with an increasing δ, verifying Eq. (2). It is pointed that although in Fig. 5(b), increasing δ appears to cause only a temperature reduction at the hot (Al) side but not a corresponding temperature increase at the cold (GaN) side, this is a statistical result in the overall initial system temperature.

To more clearly examine the effects of interfacial parameter δ, values of Kapitza conductance were calculated at various δ, and the results are shown as the data points in Fig. 5(c). Fig. 5(c) further confirms Eq. (2) that the conductance continuously increases with increasing interfacial depth. Furthermore, h_x represents the Kapitza conductance for a smooth interface at the interfacial depth $\delta = 0$. Fitting Eq. (2) to the data shown in Fig. 5(c) yields $h_x = 0.099$ $GW/m^2 \cdot K$ and $h_y = 0.065$ $GW/m^2 \cdot K$. The results calculated from Eq. (2) using these parameters are included as a straight line in Fig. 5(c). It can be seen that agreement between the MD data and the analytical model is very good. In particular, the line goes exactly through the MD data at $\delta = 0$. Fig. 5 therefore strongly verifies the analytical model.

The vertical conductance h_y is smaller than the horizontal conductance h_x. The observation that the vertical and horizontal conductances are different can be attributed to the size effects (different transport dimensions in $x-$ and $y-$ directions) and the anisotropic nature of the heat transport. In particular, Al atoms are in direct contact with both Ga and N atoms across the horizontal interfaces, but are only in direct contact with either Ga or N atoms across the vertical interface. It is possible to further test h_y and h_x in MD simulations using rotated crystal orientations so that the $y-$ axis aligns with the heat flux direction. This requires that the misfit strain, the heat transport length, and the cross section dimension are comparable to the geometry used here, which is not trivial and is left for future studies.

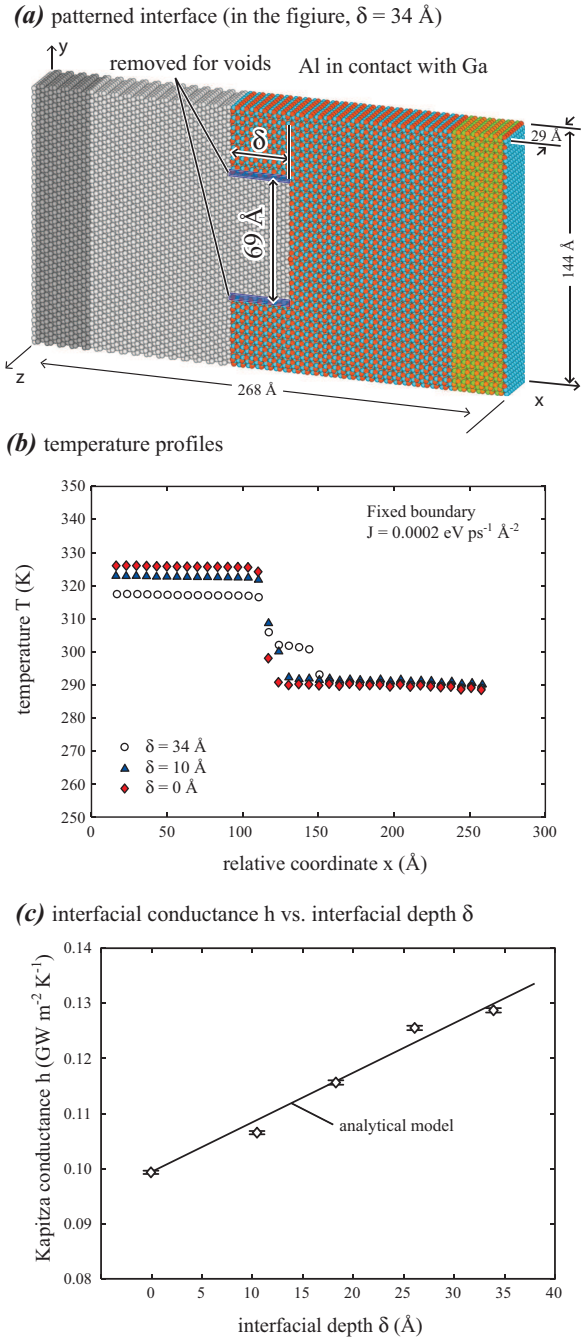

FIG. 5: (Color online) (a) Computational geometry, (b) temperature profiles, and (c) Kapitza conductance as a function of interfacial depth.

2. *Comparison of rectangular, sinoidal, and triangular morphologies of interfaces*

Effects of interfacial shape on Kapitza conductance are also studied. The systems used for this study have a length of $n_{x,Al} = 10$ and $n_{x,GaN} = 20$ (L $\approx$ 174 Å). Three interfacial morphologies corresponding to rectangular, sinoidal, and triangular shapes were used as shown in Figs. 6(a)-(c). These interfacial morphologies contain four cyclic periods along the $y-$ direction but are uniform in the $z-$ direction. Here we assume that the wave length λ and amplitude δ of the three interfaces are the same, being $\lambda = 36$ Å and $\delta = 10$ Å respectively. In addition, we assume a special interface where Al is in contact with N and the next plane of Ga has a large spacing with the contact N plane as illustrated in Fig. 6(c). This is contrary to the majority of our simulations where Al is in contact with Ga and the

next N plane has a short spacing with the contact Ga plane.

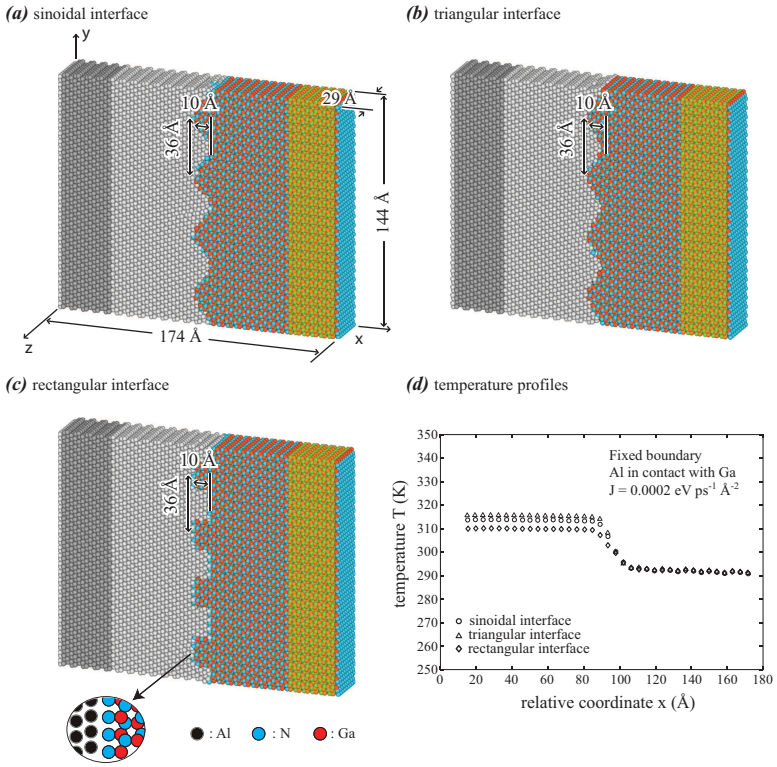

FIG. 6: (Color online) Computational geometries of (a) sinoidal, (b) triangular, and (c) rectangular shapes of interfacial morphology, and (d) the corresponding simulated temperature profiles.

Thermal transport simulations were conducted for the three interfaces at a heat flux of J = 0.0002 $eV/ps \cdot \mathring{A}^2$. The temperature profiles were calculated for the three interfaces, and the results are shown in Fig. 6(d). It can be seen that all three interfaces exhibit similar temperature profiles, namely a slow-decaying temperature within the Al and the GaN bulk, and a significant temperature drop over the 10 Å interfacial depth (δ) region. Interestingly, the overall temperature drop is least significant for the rectangular interface but most significant for the triangular interface. The Kapitza conductance values were calculated to be 0.157, 0.176, and 0.196 $GW/m^2 \cdot K$ for the triangular, sinoidal, and rectangular interface respectively. Obviously, the triangular interface has the least interfacial area and the rectangular interface has the largest interfacial area. The results that the rectangular interface has the highest Kapitza conductance and the triangular interface has the lowest Kapitza conductance are consistent with the analytical model developed in section III that Kapitza conductance increases when the total interface area increases. However, care should be taken in explaining the results because as discovered above Kapitza conductance depends on if Al is in contact with Ga or N, and the contact atoms may change at the triangular and sinoidal interfaces.

3. Interfacial wave length

To further test the analytical model developed in section III, we study the effects of interfacial wave length of the rectangular interface shown in Fig. 6(c). Starting with the same dimensions of the system as shown in Fig. 6(c), five samples with zero, one, two, three, and four periods of the rectangle teeth are uniformly created along the $y-$direction. Thermal transport simulations were conducted at a flux of J = 0.0002 $eV/ps \cdot \mathring{A}^2$. The values of Kapitza conductance were calculated. The results are shown in Fig. 7. It can be seen that Kapitza conductance nearly linearly increases as the number of period n increases from 0 to 3, and the line shown in Fig. 7 is again calculated from the analytical model described in section III. In particular, the line is seen to go almost perfectly through the data point at $n = 0$, verifying that the conductance equals h_x for flat interfaces. Furthermore, a fit of the linear relationship shown in Fig. 7 results in a horizontal conductance values of $h_x \approx = 0.17\ GW/m^2 \cdot K$, and a vertical conductance value of $h_y \approx = 0.07\ GW/m^2 \cdot K$. These are in very good agreement with $h_x \approx = 0.172\ GW/m^2 \cdot K$ (for the Al-N contact case) discussed in Fig. 4(b), and $h_y \approx = 0.065\ GW/m^2 \cdot K$ determined from Fig. 5(c) for the conductance

vs. roughness depth δ series. These observations further verify the analytical model that the increased conductance due to roughness is caused by the additional heat flow in the vertical direction.

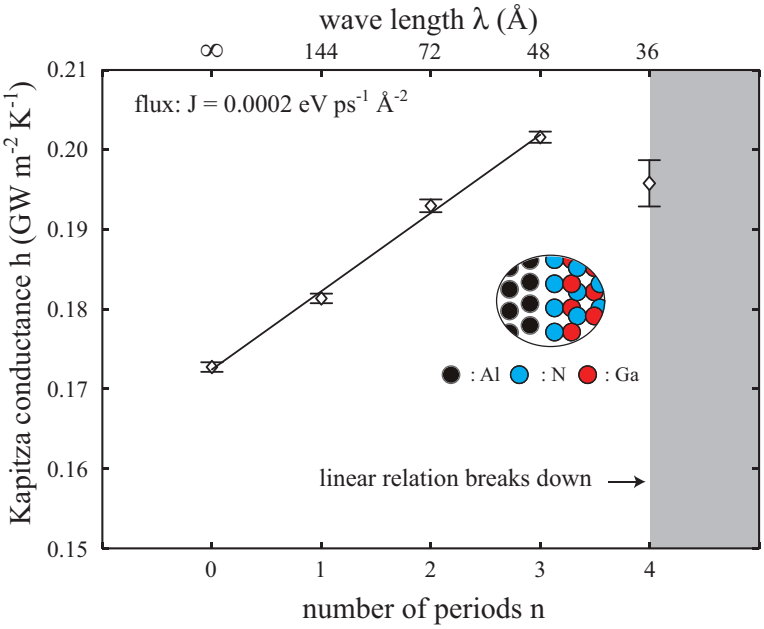

FIG. 7: (Color online) Kapitza conductance as a function of number of periods of the rectangular interfaces. Number of periods relates to roughness wave length λ defined in Figs. 3 and 4.

It is seen from Fig. 7 that when the number of period increases to 4, the linear relation starts to break down. Obviously, the linear increase of the overall interfacial conductance with overall interfacial area requires that the local interfacial conductance (contribution from local interfacial area) remains constant. This is likely to be violated because when the neighboring teeth become too close, the phonon scattering at the neighboring interfaces interact severely. While these again verify the analytical model, they show that Kapitza conductance only linearly increases with the total interfacial area when the local interfacial features do not interact and the limit to this trend is only achieved at the nanoscale.

4. Verification with the Lennard-Jones system

In order to further generalize our results, we have studied the effect of rectangular morphologies at a mass-mismatched A/B Lennard-Jones (LJ) type interfaces using a similar approach described previously[32,60]. The computational cells contain $8 \times 8 \times 80$ conventional unit cells (5.25 Å/cell) of an fcc crystal with 20,480 atoms. One half of the atoms are A-type and the other half are B-type, separated by an interface at the midpoint of the computational cell in the $x-$ direction. A- and B-type atoms are distinguished only by their masses (40 and 120 amu, respectively). All interactions are described by the 6-12 LJ potential, $E_{LJ}(r) = 4\epsilon\left[(\sigma/r)^{12} - (\sigma/r)^{6}\right]$, where r is the interatomic separation, and σ and ϵ are the LJ length and energy parameters. Ar parameters of $\sigma = 3.37$ Å and $\epsilon = 0.0103$ eV[61] are used for A-A and B-B interactions. For the A-B cross interaction, the same length parameter is used but the energy parameter is set to 0.5 ϵ and 1.0 ϵ respectively for simulating both weakly and strongly bonded interfaces. The cutoff distance is always set to $r_c = 2.5\sigma$. Conductances were calculated at 10 K. A particularly low temperature was chosen for study because we found that at temperatures above 50 K, the overall thermal resistance of the materials becomes greater than the interfacial resistance, thereby substantially decreasing the sensitivity to Kapitza conductance and leading to much larger statistical / systematical errors. Note also that while 10 K might be a low absolute temperature, it is not very low with respect to the melting temperature (approximately 12 % of the melting temperature of the LJ solids). As a result, the heat transport is not dominantly ballistic, as demonstrated using heat flux correlations by Kaburaki et al[62].

For flat interfaces, Kapitza conductance values of h = 0.038 $GW/m^2 \cdot K$ and 0.053 $GW/m^2 \cdot K$ were obtained for the weakly and the strongly bonded interfaces, respectively. In this particular case, the strongly bonded interface has a higher Kapitza conductance although this trend was found to saturate by a previous study[33]. Simulations were

performed for the weakly bonded interfaces with the rectangular morphology at different rectangular depths δ and a fixed rectangular width of $\lambda = 4$ unit cells and a fixed number of rectangular periods of $n = 1$, or at different number of periods n and a fixed width of $\lambda = 4$ unit cells and a fixed depth of $\delta = 8$ unit cells. The calculated Kapitza conductance as a function of depth δ and number of periods n are shown respectively in Figs. 8(a) and 8(b). Fig. 8(a) indicates a nearly linear increase in Kapitza conductance with increasing interfacial depth, δ. Similarly, Fig. 8(b) also shows a nearly linear increase in Kapitza conductance with increasing number of periods until the number of periods reaches four where the linear relationship breaks down because the neighboring rectangles start to interact. These results are consistent with the observations made in the Al/GaN system, and once again demonstrate that conductance increases with an increase in total interface area.

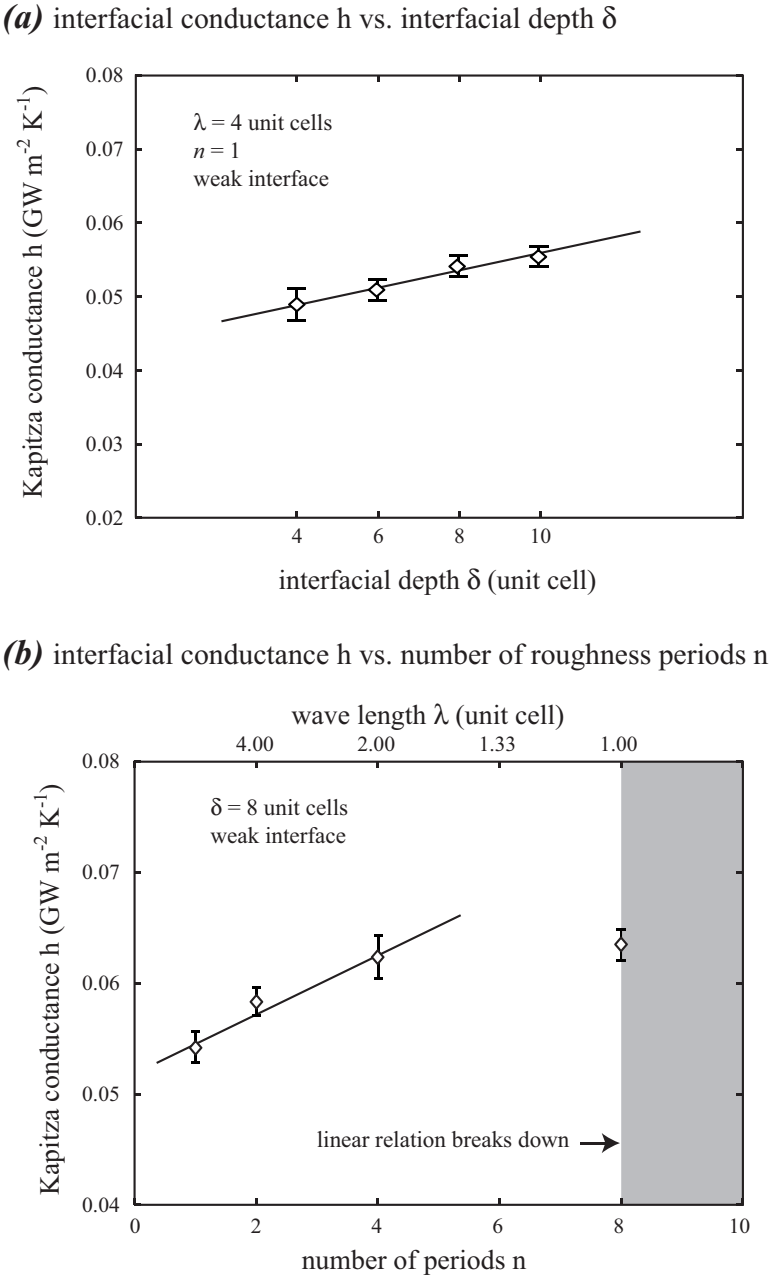

FIG. 8: Kapitza conductance as a function of (a) interfacial depth and (b) number of periods of the rectangular interfaces in the Lennard-Jones system. Number of periods relates to roughness wave length λ. Roughness depth δ and wave length λ are defined in Figs. 3 and 4.

B. Effects of interfacial voids, flux direction, and interatomic potential

Experiments performed on an Al/Si system by Hopkins et al[5] indicate that Kapitza conductance decreases when an etching process is used to modify the Si surface prior to Al deposition. The etching processes increase the interfacial roughness, which is accompanied by an increase in interfacial area. The simulated results discussed above would indicate an increase in Kapitza conductance. Note, however, that the etching process may alter the interfacial chemistry. It can also create defects, especially voids near the interfaces. While it is difficult to separate multiple factors in experiments and inappropriate to compare directly the experimental Kapitza conductance vs. interfacial roughness data with the simulated results, MD simulations can be easily used to explore the effects of voids. As a simple example, interfacial voids at the horizontal Al/GaN interfaces are created by removing ∼3 Å thick Al atoms in the blue-shaded regions in Fig. 5(a). Voids at the horizontal interfaces were studied because (1) they effectively test the analytical model on the role of the horizontal interfaces; and (2) due to a shadowing effect, voids are most likely to form at the growth surfaces that are oblique to the deposition flux[63,64], which is likely to be the case for the horizontal GaN surface when Al is deposited on the roughened GaN. The same set of simulations as those explored in Fig. 5(c) were repeated. Results of the Kapitza conductance are shown in Fig. 9 using the filled diamonds and the blue solid line, where the void-free data shown in Fig. 5(c) are reproduced using the unfilled diamonds and the red solid line. Both red and blue lines are calculated using the analytical function, Eq. (2). It can be seen that all lines going through precisely the points at $\delta = 0$, matching well the analytical model. Furthermore, the MD data with the voids is insensitive to the interfacial depth δ. This is because the voids effectively eliminate the heat transfer through the horizontal interfaces so that the total effective interfacial area is all from the vertical interfaces which is not changed by δ. This again matches well the analytical model. These observations suggest that care should be taken in trying to improve Kapitza conductance using interface roughening because experimental roughening techniques, such as etching, often cause other defects such as voids and reductions of coherence at interfaces. In such cases, the increase in the conductance due to an increase in interfacial area may be overwhelmed by the increased scattering due to increased interfacial defects.

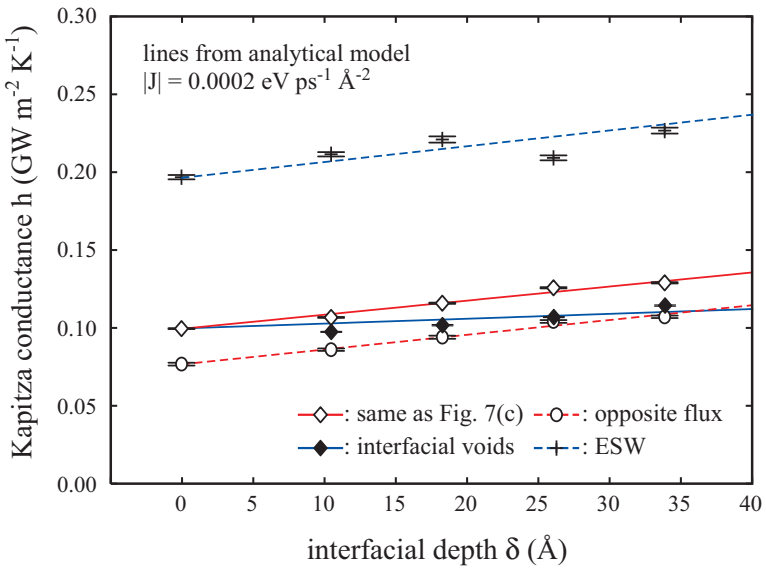

FIG. 9: (Color online) Effects of interfacial voids, heat flux directions, and interatomic potentials (metal elastic constants) on Kapitza conductance as a function of interfacial depth.

The simulations presented in the paper generally assume that the heat flux flows from Al to GaN, i.e., the hot region is at the Al end and the cold region is at the GaN end. As a special case, effects of reversing the heat flux is also studied at various interfacial depths using the same system dimensions and the same magnitude of heat flux. The calculated Kapitza conductance values are shown in Fig. 9 using the unfilled circles and the red dash line calculated from Eq. (2). It can be seen again that the Kapitza conductance increases with an increasing interfacial depth and the MD data are well captured by the analytical expression. The data derived from the two flux directions, however, differ by almost a constant over the entire interfacial depth range. This is not surprising because the two materials are not symmetric and the flux directions represent distinguishing conditions. However, care should be taken to conclude that the flux direction affects Kapitza conductance in the experimental conditions considering that the magnitude of flux (which relates to temperature gradient) used in simulations is orders of magnitude higher than those in experiments.

This is because intuitively, the effects of heat flux direction, if any, should decrease with the magnitude of the flux because a flux would lose its directionality in the limit of a zero flux. This issue will be further addressed below.

Our studies generally use the SW potential. As a special case, the ESW potential was also used to calculate Kapitza conductance as a function of interfacial depth δ under the same other conditions, and the results are included in Fig. 9 using the symbol "+" and the blue dash line defined by Eq. (2). It can be seen that the trends of Kapitza conductance vs. interfacial depth predicted by the ESW potential are the same as those predicted by the SW potential. The analytical function, Eq. (2), again captures well the MD data with the function going through precisely the MD data point at $\delta = 0$. The ESW data, however, are larger than the SW data by almost a constant over the entire depth range explored in Fig. 9. As can be seen from Eq. (2), this indicates that the difference between the ESW and SW models come from the horizontal conductance h_x, but not the vertical conductance h_y. Note that the main difference between the two potentials is that the SW potential predicts higher Al elastic constants than the ESW potentials, Appendix C. Exactly how material properties affect the interfacial conductance, however, requires dedicated studies. This will be explored extensively in another paper. The fact that the general trends are independent of the potentials provides strong verification of the robustness of our analytical model.

C. Local density of states

Using methods to extract the local phonon density of states (DOS) similar to those employed previously[32], we examined the transition of the DOS for atomic layers near the Al-GaN interface. The local DOS was obtained by taking a time sequence of velocity samples over a region transversing the Al-GaN interface (e.g., the two brown shaded regions in Fig. 3), segregating these samples into atomic layers, and averaging over time (9×2^{19} steps). Fig. 10 shows the transition from Al (layers with indices less than 0) acoustic signature to the GaN (layers with indices greater than zero) acoustic/optical signatures. The velocities for only one sample region for the flat interface are used for Fig. 10, since the corresponding DOS for the two sample regions of the toothed configuration shown in Fig 3 are similar.

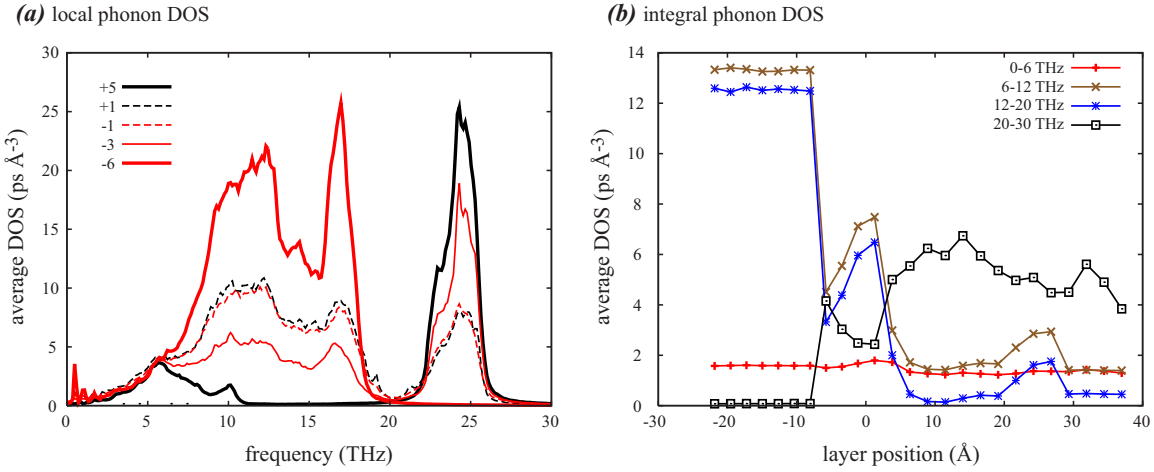

FIG. 10: (Color online) (a) Local phonon DOS, and (b) the average density in a sequence of frequency bands as a function of distance from the interface. Note that in (a) negative indices correspond to the Al side and positive indices to the GaN side. The layer indices in (a) correspond to the index of the data points in (b), where the average values of the DOS is plotted with respect to layer position. For reference, the Debye frequency for SW Al is 23.2 THz and 16.6 THz for GaN.

Figs. 10(a) and 10(b) indicate that for frequencies below about 6 THz, the DOS for each layer are essentially identical. In addition, the DOS for the Al and GaN layers nearest the interface are very close. It is noted that states in the optical range of the GaN persist approximately 5 layers into the Al side, and likewise, the full transition to Al acoustic signature is gradual. As Fig. 10(b) shows, the transition is not entirely smooth and is abrupt especially for the modes in the high acoustic range of Al. The transition length appears to be much larger than either the range of the potentials, which is at most 4.2 Å, or the tooth depth (since the transition for samples in Fig. 3 are essentially the same as in the flat interface shown). Also, it is apparent that modes in the optical range of GaN can be enhanced near the interface before relaxing to the bulk DOS and states can appear in the GaN band gap (approximately 12-20 THz) and above the bulk Al cutoff (at about 20 THz). The fact that this effect is qualitatively independent of the presence of a corrugated interface gives support to the finding that the interface conductances at this scale are properties that scale with true surface area.

As already mentioned, the GaN has its c-axis and the Al has a (111) direction normal to the interface. However, the Al and the GaN layers are strained along the interface to accommodate lattice mismatch. Although the strain is small, it makes the Al triclinic which gives a basis for interpreting the modes in the optical range of GaN on the Al as acoustic branches that are folded back over in the smaller Brillouin zone resulting from using a bigger unit cell. Apparently this effect is not the cause of the states in the GaN optical range on the Al side since these states subside far from the interface. Also, it is apparent from Fig. 10 that the two materials have similar populations of low frequency modes. Lastly, the distinct increase in the DOS in the frequency bands 6-12THz and 12-20THz for layers in the range of 20 to 30 Å into the Al side may be due to the presence of localized, anharmonic modes.

D. Wave packet analysis

To supplement the conductivities measured using the direct method with frequency-dependent information, the multiple wave-packet method[65] is used to measure the effects of interfacial shape on the transmission of normally incident acoustic phonons. As above, the systems have a cross-sections of $n_{y,Al} = 29$ and $n_{z,Al} = 10$, or $n_{y,GaN} = 26$ and $n_{z,GaN} = 9$ (t×W $\approx 144\times29$ Å^2). However, the Al and the GaN regions of the bicrystal are extended along the $x-$ direction to accommodate the large spatial extent (~ 250 cubic layers in Al) of each wave-packet. In the long $x-$ direction, the Al side is extended to contain 500 simple cubic layers while the GaN side is extended to contain 500 wurtzite [0001] layers. The MD initial conditions are calculated from a superposition of normally incident modes having wave-vector (k_x00) with k_x varying. Wave-packets comprised of modes from the single longitudinal acoustic (LA) branch and the two degenerate transverse acoustic (TA) branches are used in this work. The degenerate TA branches are sampled by creating wave-packets with polarization vectors along the y direction (Al $[\bar{1}\bar{1}2]$) and a second set of wave-packets polarized along z (Al $[2\bar{2}0]$). They all propagate along the positive $x-$ direction, reaching the interface to be either transmitted to the GaN side or reflected back to the Al side. By calculating time-dependent normal mode amplitudes at particular simulation times, the phonon transmission coefficient τ is obtained. We define τ as the ratio of the energy transmitted through the interface in a given range of frequency to the energy incident on the interface in the same frequency range.

The transmission coefficient for the Al [111] acoustic branches for planar interface and the rectangular morphology are compared in Figure 11. The transmission coefficients for longitudinal wave packets are essentially identical for both interfaces with only very slightly reduced transmission from the rectangular interface. For these wave packets, which are comprised of only modes polarized along the normal direction, the scattering is to a large extent insensitive to structure in the interface along this normal direction agreeing to within 3 % for all frequencies. This information suggests that the increased conductance of the corrugated interface is not due to increased transmission of the LA modes.

For the TA modes, a more pronounced difference is seen between the two interfaces. The rectangular interface shows higher transmission for both the lowest and highest frequencies irrespective of the polarization of the wave-packets. The transmission across each interface appears insensitive to the polarization at the highest frequencies although this trend is not observed for the lowest frequency wave-packet. The planar interface has the larger reflection (smaller transmission) for both TA polarizations. In each of these cases, the wave-packet is reflected directly back with $k_y = 0$ and $k_x \rightarrow -k_x$ upon scattering at the interface. For the rectangular interface, a more complicated interaction is seen. Both TA polarizations for the rectangular interface reflect back into multiple modes. Each polarization reflects directly back as with the planar interface in addition to scattering into branches with nonzero $k_y = \pm 0.0437$. Although the outgoing modes for each polarization are identical, the outgoing amplitudes are not. The TA y packet scatter predominantly directly back ($k_y = 0$) with two smaller outgoing wave-packets with nonzero k_y. The TA z packet scatters predominantly into the mode with $k_y = -0.0437$. The increased transmission of the TA y packet relative to the TA z one is perhaps not surprising since the displacements along y are normal to portions of the rectangular interface while displacements along the z direction are always in-plane.

The differences in scattering for the TA branches indicate that the rectangular interface enhances phonon transmission for modes that are not polarized exclusively along the long direction of the system. Enhanced transmission across an interface implies a larger Kapitza conductance[66], supporting the direct method MD results that the rectangular interface has a higher conductance than the planar one.

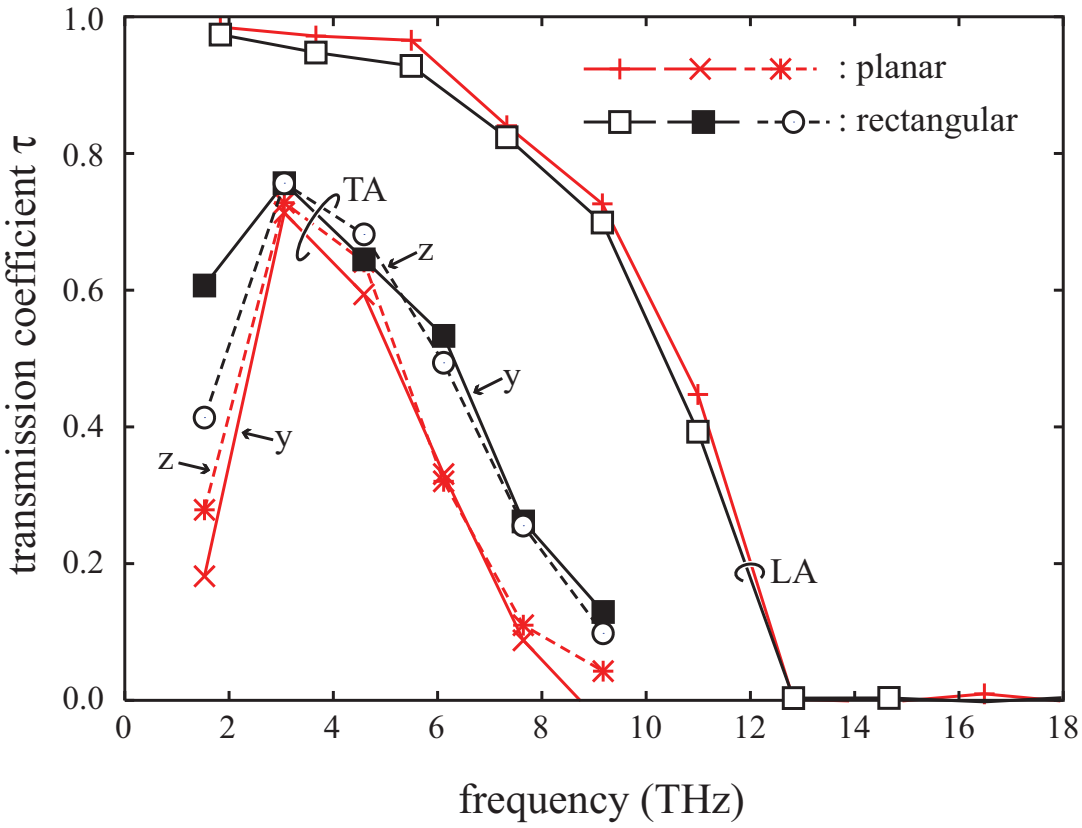

FIG. 11: (Color online) The transmission coefficient as a function of incident wave packet frequency for the planar (red) and rectangular (black) morphologies. The lines serve to guide the eyes; they are not meant to imply any structure in the curves.

V. DISCUSSION

A. Effects of interfacial disorder

In practical devices, the interfaces do not always maintain atomically sharp configurations as studied in the above. Two interfacial conductance simulations, one using a sharp interface, the other using a diffused interface, were therefore performed to explore the difference. The computational system has a cross-section dimension of $n_{y,Al} \times n_{z,Al} = 29 \times 10$ or $n_{y,GaN} \times n_{z,GaN} = 26 \times 9$ (t×W $\approx 144 \times 29$ Å^2), and a length of $(n_{x,Al}, n_{x,GaN}) = (14,28)$ (≈ 244 Å). To create a diffused interface, positions of some Ga, N and Al atoms near the interface are exchanged. The resulting diffused interface is shown in Fig. 12. Using an averaging time of 110 ns and a flux of J = 0.00012 $eV/ps \cdot \mathring{A}^2$, the temperature profiles obtained from the sharp and diffused interfaces are shown in Fig. 13 with open circle and filled diamonds, respectively. The Kapitza conductance h calculated from the temperature profiles are also indicated. It can be seen from Fig. 13 that the interfacial disorder causes a reduction of the temperature drop at the interface, and as a result, the Kapitza conductance increases from 0.084 $GW/m^2 \cdot K$ for the sharp interface to 0.135 $GW/m^2 \cdot K$ for the diffused interface. Similar enhancement of Kapitza conductance has been observed in previous MD simulations, which is attributed to a phonon bridging effect[67,68]. In this case, an intermediate layer forms at the interface where phonon properties (modes) of both Al and GaN are mixed, resulting in some average phonon dispersion that promotes thermal transport. This differs from the macroscopic concept that variable surface geometry increases "actual" area.

B. Mechanisms of conductance enhancement

The analytical model discussed in Section III and the subsequent data from molecular dynamics indicate that increasing the total interface area yields higher Kapitza conductances in both the Al/GaN and Lennard-Jones material

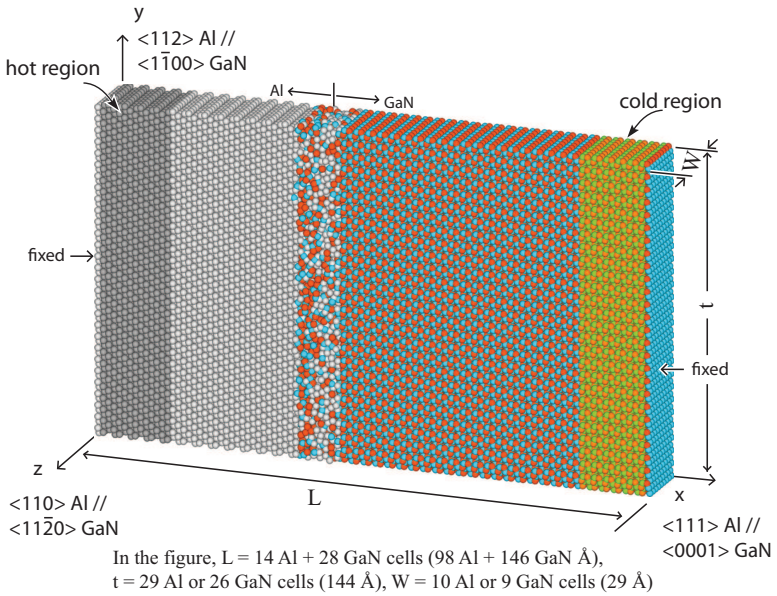

FIG. 12: (Color online) Computational geometry of a disordered interface.

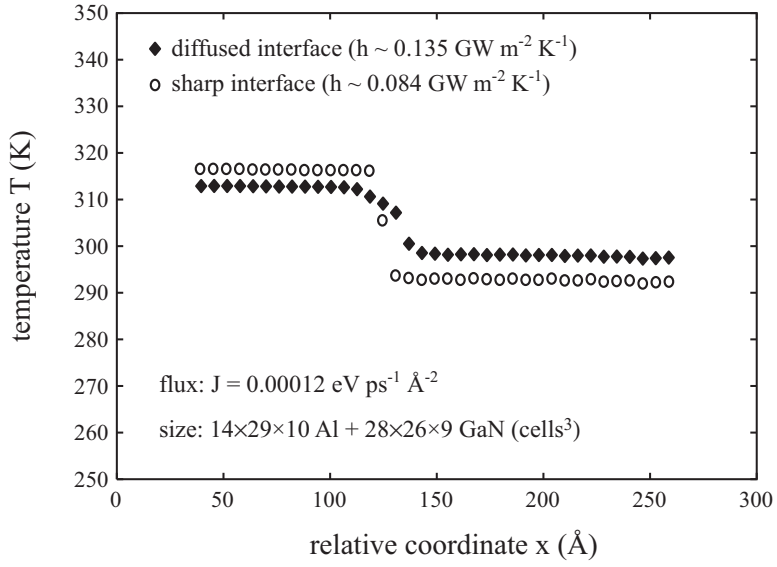

FIG. 13: Comparison of temperature profiles between sharp and diffused interfaces.

systems. However, it may come as a surprise that such a "macroscopic" principle holds at the nanoscale. In addition, Figs. 12 and 13 indicate that a diffused interface can cause an increase in conductance without changing the total interface area. To consolidate these complicated phenomena, we once again turn to the Lennard-Jones system. By averaging the kinetic energy of each atom from a periodic sampling of data taken over 6 million time steps, atom-by-atom temperature profiles at weakly- ($\epsilon_{AB} = 0.5\ \epsilon$) and strongly- ($\epsilon_{AB} = \epsilon$) bonded LJ interfaces were obtained for two different rectangular morphologies ($\lambda = 2$ and 4 unit cells respectively with a fixed $\delta = 4$). The results are shown in Fig. 14.

Examinations of the uniformity of the temperature profiles on either side of the interface in each of the separate profiles gives an insight on two possible mechanisms for conductance enhancement. In the cases of wider teeth or weakly-bonded interfaces (lower left frame in Fig. 14), the temperature distributions on each side of the interface are more uniform and the temperature drop across the interface is large on both the vertical and horizontal interfaces. This result once again supports the discussion above that any observed increase in conductance can be attributed to an increase in total interface area. However, in the case of strongly-bonded interfaces with narrower teeth (upper

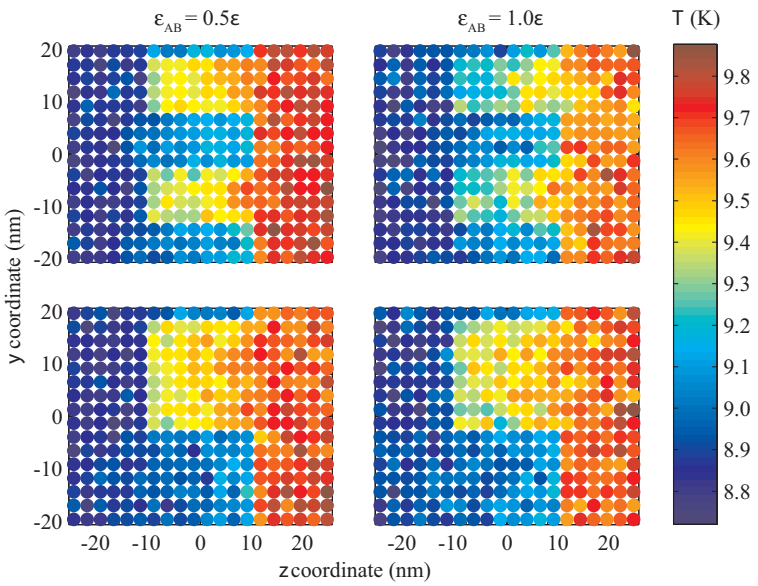

FIG. 14: (Color online) Atom-by-atom temperature profiles at Lennard-Jones type interfaces for (left) weakly- and (right) strongly-bonded interfaces with two different rectangular morphologies.

right in Fig. 14), the temperature profiles are less uniform on either side of the interface and the temperature drop at the vertical and horizontal interfaces becomes less apparent. This suggests that for strongly-bonded interfaces with small interfacial features, the observed enhancement can be attributed to a "phonon bridge" effect rather than an increase in total interface area[67–69]. That is, by nanostructuring the interface, a spatially-graded region exists where the vibrational properties overlap those of both materials A and B.

C. Effects of heat flux direction

As discovered above, Fig. 9 appears to show different values of Kapitza conductance for the two opposite flux directions at the simulated magnitude of flux. This phenomenon warrantees further studies as the magnitude of heat flux used in experiments is significantly smaller. Here we perform two series of simulations with opposite flux directions at different magnitudes of flux of $|\mathrm{J}| = 0.00005$, 0.00010, and 0.00015 $eV/ps \cdot \mathring{A}^2$. The system sizes used are the same as those in Fig. 5(a), namely the cross-section dimensions have $n_{y,Al} = 29$ and $n_{z,Al} = 10$, or $n_{y,GaN} = 26$ and $n_{z,GaN} = 9$ (t×W $\approx 144\times29$ Å^2), and the length dimension has $n_{x,Al} = 16$ and $n_{x,GaN} = 30$ (L ≈ 268 Å). A flat interface with $\delta = 0$ is assumed. A Kapitza conductance was calculated for each simulation and the results are shown in Fig. 15 using unfilled diamonds and unfilled circles to represent respectively the Al→GaN and the GaN→Al flux directions. Fig. 15 clearly indicates that the opposite heat fluxes produce different values of Kapitza conductance at a large magnitude of flux, corroborating the results shown in Fig. 9. However, this difference monotonically reduces when the magnitude of the flux is reduced. Fig. 15 also appears to indicate that the values of Kapitza conductance for the two flux directions will converge to the same value in the limit of $|\mathrm{J}| \to 0$. All these observations can be expected from the physical intuition. It is reasonable that at the experimental heat fluxes which are significantly smaller in magnitude than the simulated fluxes, the effect of flux direction is negligible and the same Kapitza conductance should be measured in both flux directions.

Pursuing small magnitudes of fluxes in simulations is not feasible as it will rapidly increase the statistical / systematical errors. For particular systems such as an Al/GaN interface, Fig. 15 indicates that the values of Kapitza conductance obtained from the opposite flux directions deviate from the $|\mathrm{J}| \to 0$ value in opposite directions. As a result, one effective method to reduce the effect of finite flux magnitude is to perform calculations in both flux directions and then take the average conductance of the two calculations. It remains to be seen if this holds for other interfacial systems.

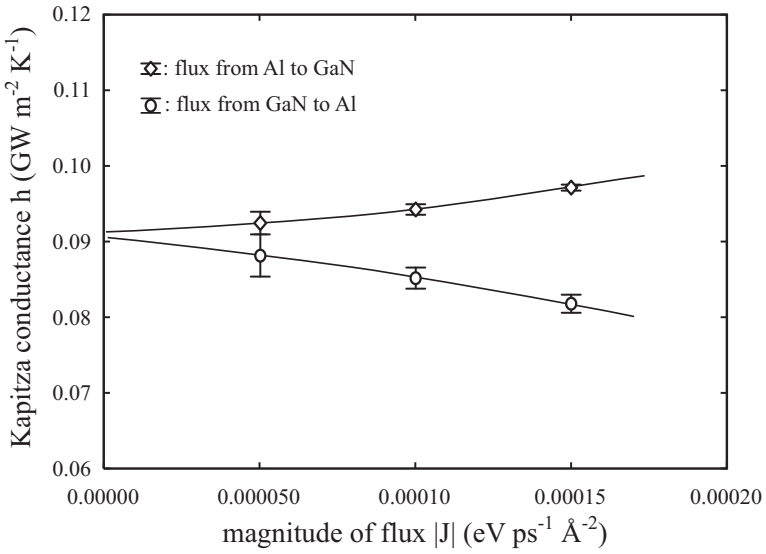

FIG. 15: Kapitza conductance as a function of magnitude of flux in two opposite flux directions.

VI. CONCLUSIONS

A relatively thorough molecular dynamics study of effects of interfacial morphology on thermal boundary conductance has been performed. Highly accurate results are achieved using extremely large direct method MD simulations, and general conclusions are ensured using three different types of interatomic potentials. We found that for weakly bonded ideal interfaces with large roughness wave length (can be in the nanometer range), the interface boundary conductance is proportional to the total interfacial area and hence increases with interfacial roughness. This phenomenon is corroborated using a variety of conditions including different interfacial roughness depth, wave length, shape, presence of voids, and interatomic potential. On the other hand, we found that for strongly bonded interfaces and narrower roughness wave length, this linear relationship with the interfacial area breaks down. However, such narrower roughness wave length may cause diffused interface, activating a "phonon bridge" effect that also increases thermal boundary conductance. Wave packet analysis indicates that the observed increase in thermal boundary conductance in the rectangular interface mainly comes from the transverse acoustic modes.

Acknowledgments

Sandia National Laboratories is a multi-program laboratory managed and operated by Sandia Corporation, a wholly owned subsidiary of Lockheed Martin Corporation, for the U.S. Department of Energy's National Nuclear Security Administration under contract DE-AC04-94AL85000. This work was performed under a Laboratory Directed Research and Development (LDRD) project. PEH is also appreciative for funding from NSF Grant number CBET 1134311.

Appendix A: Al-Ga-N Stillinger-Weber (SW) potential

According to the SW potential[38], the total system energy is expressed as

$$E = \frac{1}{2}\sum_{i=1}^{N}\sum_{j=i_1}^{i_N}\left[\phi_{IJ}\left(r_{ij}\right) + u_{IJ}\left(r_{ij}\right)\sum_{k=i_1,\ k\neq j}^{i_N} u_{IK}\left(r_{ik}\right)\left(cos\theta_{jik} + \frac{1}{3}\right)^2\right] \tag{A1}$$

where i_1, i_2, ..., i_N is a list of neighbors to atom i, θ_{jik} is the bond angle formed by atoms j and k at the site of atom i, $\phi_{IJ}\left(r_{ij}\right)$ and $u_{IJ}\left(r_{ij}\right)$ are two pair functions of atomic spacing r_{ij} with subscripts ij and IJ indicating respectively the pair of atoms and the species of the pair of atoms. Here $\phi_{IJ}\left(r_i j\right)$ and $u_{IJ}\left(r_i j\right)$ are expressed as

$$\phi_{IJ}\left(r\right) = A_{IJ}\cdot\epsilon_{IJ}\left[B_{IJ}\left(\frac{\sigma_{IJ}}{r}\right)^4 - 1\right]\exp\left(\frac{\sigma_{IJ}}{r - a_{IJ}\cdot\sigma_{IJ}}\right) \tag{A2}$$

TABLE I: SW potential parameters.

parameter	GaGa	NN	AlAl	GaN	GaAl	NAl
ϵ (eV)	1.2000	1.2000	0.5650	2.1700	0.5223	1.4400
σ (Å)	2.1000	1.3000	2.6674	1.6950	2.7322	1.6414
a	1.60	1.80	1.55	1.80	1.55	1.80
λ	32.5	32.5	0.0	32.5	0.0	32.5
γ	1.2	1.2	1.2	1.2	1.2	1.2
A	7.9170	7.9170	17.8118	7.9170	17.8118	7.9155
B	0.72	0.72	0.72	0.72	0.72	0.72

and

$$u_{IJ}(r) = \sqrt{\lambda_{IJ} \cdot \epsilon_{IJ}} \exp\left(\frac{\gamma_{IJ} \cdot \sigma_{IJ}}{r - a_{IJ} \cdot \sigma_{IJ}}\right) \tag{A3}$$

where ϵ, σ, a, λ, γ, A and B are pair dependent parameters.

Our previous molecular dynamics simulations on thermal transport in GaN[51,55,56] have applied the GaN Stillinger-Weber (SW) potential[38] parameterized by Béré and Serra[70,71]. To generate a consistent set of data, the same GaN potential is used in the present study to model the semiconductor layer. With the GaN SW potential known, we need to determine seven parameters σ_{IJ}, ϵ_{IJ}, a_{IJ}, λ_{IJ}, γ_{IJ}, A_{IJ}, B_{IJ} for each of the remaining three pairs $IJ = AlAl$, GaN, and NAl in the Al-Ga-N system. Note that for any elemental systems, the SW potential has a special feature that the lattice constant scales with the parameter σ and the cohesive energy scales with the parameter ϵ. If only σ and ϵ are changed, the order of cohesive energies of different phases remains unchanged because these cohesive energies all scale with ϵ. This means that σ and ϵ can be easily re-scaled to match the lattice constant and the cohesive energy of different materials without re-parameterization. For instance, our calculations indicated that for the GaN SW potential[70,71], the lowest-energy Ga crystal is fcc with a lattice constant of 3.729 Å and a cohesive energy of -1.437 eV/atom. Experimentally, the lowest-energy Al phase is also fcc but with a different lattice constant of 4.050 Å and a different cohesive energy of -3.390 eV/atom[72]. We can therefore simply scales the parameters σ_{GaGa} and ϵ_{GaGa} by factors of 4.050/3.729 and 3.390/1.437 to get the parameters σ_{AlAl} and ϵ_{AlAl}. This ensures that the fcc crystal remains to be the lowest-energy phase for Al with precise experimental lattice constant and cohesive energy. Similar approach can be used for materials with other crystal structures. For example, Si has a dc crystal structure and Si SW potential has been well developed[38]. One can create a SW potential for any dc material with arbitrary lattice constant and cohesive energy by simply re-scaling the Si SW potential parameters[38]. This is also applicable to the parameters between dissimilar species in a binary compound. In this work, however, we have refitted the parameters.

According to the literature convention for SW potentials and the GaN potential by Béré and Serra[70,71], we set universal parameters $\gamma_{IJ} = 1.2$ and $B_{IJ} = 0.72$ ($IJ = AlAl$, GaN, NAl). A universal value of $\lambda_{NAl} = 32.5$ is also used for the NAl pair. However, we set $\lambda_{AlAl} = \lambda_{GaAl} = 0$ for the $AlAl$ and $GaAl$ pairs so that these two pair interactions are angular independent [see Eqs. (A1) and (A3)], which is sufficient to describe the fcc Al and GaAl crystals. We selected the parameter a_{IJ} ($IJ = AlAl$, GaN, NAl) intuitively based on the corresponding values for the GaN system (a is related to the cutoff distance of the potential and is usually also chosen rather than fitted in literature SW potentials). We then fit the remaining parameters to the experimental lattice constants and cohesive energies of the fcc Al, wz AlN and fcc AlGa phases under the constraints that the equilibrium fcc Al and wz AlN phases have the lowest energy compared with their other structures. The results of the parameterization, along with the GaN parameters[70,71], are summarized in Table I.

Appendix B: Al-Ga-N Hybrid EAM+SW (ESW) potential

For the hybrid EAM+SW (ESW) Al-Ga-N model, we use a well established EAM Al potential[73] to describe Al-Al interactions, the literature SW Ga-N potential[70,71] to describe the Ga-Ga, N-N, and Ga-N interactions, and a Morse potential to describe the Al-Ga and Al-N cross interactions. Only the Morse potential for the cross interactions needs to be developed. The Morse potential is expressed as

$$E_{IJ}(r_{ij}) = -E_{b,IJ} \cdot \{\exp[-2\alpha(r_{ij} - r_{0,IJ})] - 2\exp[-\alpha(r_{ij} - r_{0,IJ})]\} \tag{B1}$$

where E_b and r_0 are bond energy and bond length respectively, and α is a parameter. To fully define the Al-N and Al-Ga Morse potentials, we will need to determine eight parameters $r_{0,AlGa}$, $E_{b,AlGa}$, $r_{0,AlN}$, $E_{b,AlN}$, α_{AlGa},

TABLE II: Cross interaction parameters of the ESW potential.

IJ	$r_{0,IJ}$	$E_{b,IJ}$	α_{IJ}	$r_{c,IJ}$
GaAl	2.933	−0.520	1.979	5.260
NAl	1.892	−1.440	2.085	4.101

TABLE III: Cohesive energies E_c (eV/atom) of different phases. dc: diamond-cubic, sc: simple-cubic, bcc: body-centered-cubic, fcc: face-centered-cubic, zb: zinc-blende, wz: wurtzite.

		cal.					exp.	
elemental systems								
system	potential	dimer	dc	sc	bcc	fcc	phase	E_c
Al	SW	−0.28	−1.13	−1.70	−3.33	−3.39	fcc	−3.39[a]
Al	ESW	−0.92	−2.47	−2.96	−3.25	−3.36	fcc	−3.39[a]
Ga	SW,ESW	−0.33	−1.31	−1.33	−1.42	−1.44	α	−2.81[b]
N	SW,ESW	−0.60	−2.40	−2.03	−1.96	−1.90	N_2	−4.96[b]
compound systems								
system	potential	dimer	zb	wz	CsCl	NaCl	phase	E_c
GaN	SW,ESW	−1.09	−4.34	−4.34	−3.21	−3.67	wz	−4.53[c]
AlN	SW	−0.72	−4.43	−4.43	−2.91	−4.05	wz	−5.76[d]

[a] from reference[72]
[b] from reference[75]
[c] from references[76,77]
[d] from references[78]

α_{AlN}, and cutoff distances $r_{c,AlGa}$ and $r_{c,AlN}$. To produce similar cross interactions to those of the Al-Ga-N ternary SW potential, we fit $r_{0,AlGa}$, $E_{b,AlGa}$, α_{AlGa}, $r_{0,AlN}$, $E_{b,AlN}$, and α_{AlN} by matching Eq. (B1) to the corresponding pair interaction of the ternary SW potential so that at the equilibrium bond length (at which the pair energy is at minimum), both potentials give the same pair energy and the same second derivative of the pair energy. For a smooth cutoff of the potential that was found to be especially important for thermal transport studies[74], it is required that the potential function $\exp[-\alpha_{IJ}(r - r_{0,IJ})]$ drops to a small value (say $\delta = 0.01$) at the cutoff distance $r = r_c$. We can then find the cutoff distances using the equation $r_{c,IJ} = -ln(\delta)/\alpha_{IJ} + r_{0,IJ}$. The cross interaction parameters of the ESW potential thus determined are listed in Table II.

Appendix C: Characteristics of the SW and ESW potentials

To demonstrate the difference between the SW and the ESW Al-Ga-N potentials, properties of a variety of Al, Ga, N, GaN, AlN, and GaAl phases were calculated. Some selected results are summarized in Tables III- V for cohesive energies, lattice constants, and elastic constants respectively along with the corresponding available experimental data. Note that for material systems that do not involve Al, the SW and the hybrid ESW potentials are equivalent.

With the notion that SW potentials always give the same cohesive energies for the wz and the dc structures, Table

TABLE IV: Lattice constants a and c (Å) of the lowest-energy phases.

	Al (fcc)			Ga (fcc)	N (dc)	GaN (wz)		AlN (wz)	
	SW	ESW	exp.[a]	SW,ESW	SW,ESW	SW,ESW	exp.[b]	SW	exp.[c]
a	4.05	4.05	4.05	3.73	3.46	3.19	3.19	2.97	3.11
c	–	–	–	–	–	5.20	5.19	4.85	4.98

[a] from reference[72]
[b] from references[76,77]
[c] from references[79,80]

TABLE V: Single crystal elastic constants C_{ij} ($eV/\mathring{A}^3$) of the lowest-energy phases.

C_{ij}	Al (fcc)			Ga (fcc)[a]	N (dc)[b]	GaN (wz)		AlN (wz)	
	SW	ESW	exp.[c]	SW,ESW	SW,ESW	SW,ESW	exp.[d]	SW	exp.[e]
C_{11}	2.29	0.71	0.67	3.31	2.48	2.87	2.44	4.82	2.57
C_{12}	1.15	0.39	0.38	3.20	1.17	0.64	0.89	1.27	0.93
C_{13}	1.15	0.39	0.38	3.20	1.17	0.35	0.68	0.86	0.62
C_{33}	2.29	0.71	0.67	3.31	2.48	3.16	2.49	5.23	2.43
C_{44}	1.15	0.20	0.18	0.64	1.75	0.82	0.64	1.36	0.78

[a]No experimental elastic constants are available for fcc Ga as this is a fictitious phase. The bulk modulus of α-Ga is around 0.37 eV/Å^3[81,82]

[b]No experimental elastic constants are available for dc N as this is a fictitious phase. The bulk modulus of dc N calculated from density functional theory is 1.37 eV/Å^3[83]

[c]from reference[84]

[d]from reference[85]

[e]from reference[86]

III indicates that both SW and ESW potentials predict the fcc Al and wz GaN to have the lowest energy, in agreement with the equilibrium crystal structures observed in experiments. The SW potential also correctly predicts the observed wz structure of the AlN compound to have the lowest energy[72,76–78]. As expected, the ESW potential does not predict a stable wz AlN structure because the Al-N interaction is represented by an angular-independent Morse potential. Hence, no AlN properties of the ESW model are included in Tables III- V. The room-temperature, experimentally observed equilibrium phases for N and Ga are N_2 vapor and α-Ga[75]. These commonly observed equilibrium phases are not captured by either the SW[70,71] potential or the ESW potential that inherits the Ga and N properties from the SW potential (e.g., the predicted -0.60 eV energy of the N_2 is significantly higher than the predicted -2.40 eV energy of the dc structure of N). The inaccuracy in the AlN, N, and Ga phases is not particularly important for our systems where no local AlN, N and Ga regions are present.

Table IV shows that both SW and ESW potential predict well the experimental lattice constants of the equilibrium phases fcc Al and wz GaN. The SW potential also predicts reasonably well the experimental lattice constants of the equilibrium AlN phase, which is not stable in ESW calculations. Finally, Table V indicates that SW and ESW potentials predict reasonably good elastic constants for the equilibrium GaN crystal. For Al, the ESW potential predicts excellent elastic constants, whereas the SW potential significantly over-estimates the elastic constants. Note that the overestimation of the elastic constants by the SW potential is inevitable due to the short cutoff distance required by the SW potential. On the other hand, a variation of the elastic constants between the SW and the ESW potentials provides an additional means to examine the effects of elastic constants.

* X.W.Zhou:xzhou@sandia.gov

[1] P. L. Kapitza, J. Phys. (USSR) **4**, 181 (1941).
[2] E. T. Swartz and R. O. Pohl, Rev. Mod. Phys. **61**, 605 (1989).
[3] G. D. Mahan and L. M. Woods, Phys. Rev. Lett. **80**, 4016 (1998).
[4] L. W. da Silva and M. Kaviany, Inter. J. Heat Mass Transfer **47**, 2417 (2004).
[5] P. E. Hopkins, L. M. Phinney, J. R. Serrano, and T. E. Beechem, Phys. Rev. B **82**, 085307 (2010).
[6] D. G. Cahill, W. K. Ford, K. E. Goodson, G. D. Mahan, A. Majumdar, H. J. Maris, R. Merlin, and S. R. Phillpot, J. Appl. Phys. **93**, 793 (2003).
[7] H.-K. Lyeo and D. G. Cahill, Phys. Rev. B **73**, 144301 (2006).
[8] P. M. Norris and P. E. Hopkins, J. Heat Transfer **131**, 43207 (2009).
[9] E. T. Swartz and R. O. Pohl, Appl. Phys. Lett. **51**, 2200 (1987).
[10] P. E. Hopkins and P. M. Norris, Appl. Phys. Lett. **89**, 131909 (2006).
[11] P. E. Hopkins, P. M. Norris, R. J. Stevens, T. E. Beechem, and S. Graham, J. Heat Transfer **130**, 62402 (2008).
[12] B. N. J. Persson, A. I. Volokitin, and H. Ueba, J. Phys.: Condens. Matter **23**, 45009 (2011).
[13] J. C. Duda and P. E. Hopkins, Appl. Phys. Lett. **100**, 111602 (2012).
[14] P. E. Hopkins, J. C. Duda, S. P. Clark, C. P. Hains, T. J. Rotter, L. M. Phinney, and G. Balakrishnan, Appl. Phys. Lett. **98**, 161913 (2011).
[15] P. E. Hopkins, J. C. Duda, C. W. Petz, and J. A. Floro, Phys. Rev. B **84**, 035438 (2011).
[16] A. Rajabpour, S. M. V. Allaei, Y. Chalopin, F. Kowsary, and S. Volz, J. Appl. Phys. **110**, 113529 (2011).
[17] K. Termentzidis, S. Merabia, P. Chantrenne, and P. Keblinski, Int. J. Heat Mass Trans. **54**, 2014 (2011).
[18] K. Termentzidis, P. Chantrenne, and P. Keblinski, Phys. Rev. B **79**, 214307 (2009).
[19] B. C. Daly, H. J. Maris, K. Imamura, and S. Tamura, Phys. Rev. B **66**, 024301 (2002).
[20] K. Imamura, Y. Tanaka, N. Nishiguchi, S. Tamura, and H. J. Maris, J. Phys.: Condense. Matter **15**, 8679 (2003).
[21] E. S. Landry and A. J. H. McGaughey, Phys. Rev. B **80**, 165304 (2009).
[22] M. Hu, P. Keblinski, and P. K. Schelling, Phys. Rev. B **79**, 104305 (2009).
[23] P. K. Schelling, S. R. Phillpot, and P. Keblinski, J. Appl. Phys. **95**, 6082 (2004).
[24] Z.-Y. Ong and E. Pop, Phys. Rev. B **81**, 155408 (2010).
[25] S. Shin, M. Kaviany, T. Desai, and R. Bonner, Phys. Rev. B **82**, 081302R (2010).
[26] R. J. Stevens, L. V. Zhigilei, and P. M. Norris, Int. J. of Heat Mass Transfer **50**, 3977 (2007).
[27] R. J. Stevens, P. M. Norris, and L. V. Zhigilei, Proc. IMECE04 pp. 60334–9 (2004).
[28] X. W. Zhou, R. E. Jones, J. C. Duda, C. J. Kimmer, and P. E. Hopkins, unpublished (2013).
[29] M. S. W. J. Evans and P. Keblinski, Appl. Phys. Lett. **100**, 261908 (2012).
[30] C. F. Carlborg, J. Shiomi, and S. Maruyama, Phys. Rev. B **78**, 205406 (2008).
[31] S. Merabia and K. Termentzidis, Phys. Rev. B **86**, 094303 (2012).
[32] J. C. Duda, T. S. English, E. S. Piekos, W. A. Soffa, L. V. Zhigilei, and P. E. Hopkins, Phys. Rev. B **84**, 193301 (2011).
[33] M. Shen, W. J. Evans, D. Cahill, and P. Keblinski, Phys. Rev. B **84**, 195432 (2011).
[34] M. S. Dresselhaus, G. Dresselhaus, X. Sun, Z. Zhang, S. B. Cronin, T. Koga, J. Y. Ying, and G. Chen, Microscale Thermophys. Eng. **3**, 89 (1999).
[35] B. Poudel, Q. Hao, Y. Ma, Y. Lan, A. Minnich, B. Yu, X. Yan, D. Wang, A. Muto, D. Vashaee, et al., Science **320**, 634 (2008).
[36] S. B. Riffat and X. L. Ma, Appl. Therm. Eng. **23**, 913 (2003).
[37] S. M. Sze, physics of semiconductor devices (Wiley, New York, 1981).
[38] F. H. Stillinger and T. A. Weber, Phys. Rev. B **31**, 5262 (1985).
[39] M. S. Daw and M. I. Baskes, Phys. Rev. B **29**, 6443 (1984).
[40] S. M. Foiles, M. I. Baskes, and M. S. Daw, Phys. Rev. B **33**, 7983 (1986).
[41] L. Koci, E. M. Bringa, D. S. Ivanov, J. Hawreliak, J. McNaney, A. Higginbotham, L. V. Zhigilei, A. B. Belonoshko, B. A. Remington, and R. Ahuja, Phys. Rev. B **74**, 012101 (2006).
[42] L. Jiang and H. L. Tsai, J. Heat Transfer **127**, 1167 (2005).
[43] P. E. Hopkins, J. L. Kassebaum, and P. M. Norris, J. Appl. Phys. **105**, 023710 (2009).
[44] Y. Wang, X. Ruan, and A. K. Roy, Phys. Rev. B **85**, 205311 (2012).
[45] A. Majumdar and P. Reddy, Appl. Phys. Lett. **84**, 4768 (2004).
[46] T. Ikeshoji and B. Hafskjold, Mol. Phys. **81**, 251 (1994).
[47] P. K. Schelling and S. R. Phillpot, J. Am. Ceram. Soc. **84**, 2997 (2001).
[48] P. Jund and R. Jullien, Phys. Rev. B **59**, 13707 (1999).
[49] P. K. Schelling, S. R. Phillpot, and P. Keblinski, Phys. Rev. B **65**, 144306 (2002).
[50] Y. G. Yoon, R. Car, D. J. Srolovitz, and S. Scandolo, Phys. Rev. B **70**, 012302 (2004).
[51] X. W. Zhou, S. Aubry, R. E. Jones, A. Greenstein, and P. K. Schelling, Phys. Rev. B **79**, 115201 (2009).
[52] G. A. Slack, J. Phys. Chem. Sol. **34**, 321 (1973).
[53] A. A. Marmalyuk, R. K. Akchurin, and V. A. Gorbylev, High Temperature **36**, 817 (1998).
[54] B. A. Danilchenko, T. Paszkiewicz, S. Wolski, A. Jezowski, and T. Plackowski, Appl. Phys. Lett. **89**, 61901 (2006).
[55] X. W. Zhou, R. E. Jones, and S. Aubry, Phys. Rev. B **81**, 073304 (2010).

[56] X. W. Zhou, R. E. Jones, and S. Aubry, Phys. Rev. B **81**, 155321 (2010).
[57] W. G. Hoover, Phys. Rev. A **31**, 1695 (1985).
[58] K. S. Novoselov, A. K. Geim, S. V. Morozov, D. Jiang, Y. Zhang, S. V. Dubonos, I. V. Grigorieva, and A. A. Firsov, Science **306**, 666 (2004).
[59] A. R. Smith, R. M. Feenstra, D. W. Greve, M.-S. Shin, M. Skowronski, J. Neugebauer, and J. E. Northrup, Appl. Phys. Lett. **72**, 2114 (1998).
[60] J. C. Duda, C. J. Kimmer, W. A. Soffa, X. W. Zhou, R. E. Jones, and P. E. Hopkins, J. Appl. Phys. **112**, 093515 (2012).
[61] D. V. Matyushov and R. Schmid, J. Chem. Phys. **104**, 8627 (1996).
[62] H. Kaburaki, J. Li, S. Yip, and H. Kimizuka, J. Appl. Phys. **102**, 043514 (2007).
[63] U. Schulz, S. G. Terry, and C. G. Levi, Mater. Sci. Eng. A: Struct. Mater. Prop. Micro. Proc. **360**, 319 (2003).
[64] R. W. Smith and D. J. Srolovitz, J. Appl. Phys. **79**, 1448 (1996).
[65] C. Kimmer, S. Aubry, A. Skye, and P. K. Schelling, Phys. Rev. B **75**, 144105 (2007).
[66] R. J. Stoner and H. J. Maris, Phys. Rev. B **48**, 16373 (1993).
[67] T. S. English, J. C. Duda, J. L. Smoyer, D. A. Jordan, P. M. Norris, and L. V. Zhigilei, Phys. Rev. B **85**, 035438 (2012).
[68] Z. Liang and H.-L. Tsai, J. Phys.: Condens. Matter **23**, 495303 (2011).
[69] J. C. Duda, T. S. English, E. S. Piekos, T. E. Beechem, T. W. Kenny, and P. E. Hopkins, J. Appl. Phys. **112**, 073519 (2012).
[70] A. Béré and A. Serra, Phys. Rev. B **65**, 205323 (2002).
[71] A. Béré and A. Serra, Phil. Mag. **86**, 2159 (2006).
[72] J. Mei and J. W. Davenport, Phys. Rev. B **46**, 21 (1992).
[73] Y. Mishin, D. Farkas, M. J. Mehl, and D. A. Papaconstantopoulos, Phys. Rev. B **59**, 3393 (1999).
[74] X. W. Zhou and R. E. Jones, Mod. Sim. Mater. Sci. Eng. **19**, 25004 (2011).
[75] K. Albe, K. Nordlund, J. Nord, and A. Kuronen, Phys. Rev. B **66**, 035205 (2002).
[76] J. Serrano, A. Rubio, E. Hernández, A. Muñoz, and A. Mujica, Phys. Rev. B **62**, 16612 (2000).
[77] J. Nord, K. Albe, P. Erhart, and K. Nordlund, J. Phys.: Condens. Matter **15**, 5649 (2003).
[78] P. Ruterana, B. Barbaray, A. Béré, P. Vermaut, A. Hairie, E. Paumier, G. Nouet, A. Salvador, A. Botchkarev, and H. Morkoç, Phys. Rev. B **59**, 15917 (1999).
[79] K. Kim, W. R. L. Lambrecht, and B. Segall, Phys. Rev. B **53**, 16310 (1996).
[80] J. H. Edgar, ed., properties of group III nitrides (Electronic Materials Information Service Datareviews Series, Institution of Electrical Engineers, London, 1994).
[81] C. Kittel, introduction to solid state physics (Wiley, New York, 1979), 5th ed.
[82] K. R. Lyall and J. F. Cochran, Can. J. Phys. **49**, 1075 (1971).
[83] C. Mailhiot, L. H. Yang, and A. K. McMahan, Phys. Rev. B **46**, 14419 (1992).
[84] J. F. Thomas Jr., Phys. Rev. **175**, 955 (1968).
[85] K. Tsubouchi and N. Mikoshiba, IEEE Trans. Sonics Ultrasonics **SU-32**, 634 (1985).
[86] L. E. McNeil, M. Grimsditch, and R. H. French, J. Am. Ceram. Soc. **76**, 1132 (1993).